The Astrophysical Journal, 931:45 (29pp), 2022 May 20 https://doi.org/10.3847/1538-4357/ac6517

The Factory and the Beehive. IV. A Comprehensive Study of the Rotation X-Ray Activity Relation in Praesepe and the Hyades

Alejandro Núñez[1,8], Marcel A. Agüeros[1], Kevin R. Covey[2], Stephanie T. Douglas[3], Jeremy J. Drake[4], Rayna Rampalli[5], Emily C. Bowsher[1], Phillip A. Cargile[4], Adam L. Kraus[6], and Nicholas M. Law[7]

[1] Department of Astronomy, Columbia University, 550 West 120th Street, New York, NY 10027, USA; alejo.nunez@gmail.com

[2] Department of Physics & Astronomy, Western Washington University, Bellingham, WA 98225, USA

[3] Department of Physics, Lafayette College, 730 High St, Easton, PA 18042, USA

[4] Center for Astrophysics | Harvard & Smithsonian, 60 Garden St, Cambridge, MA 02138, USA

[5] Department of Physics and Astronomy, Dartmouth College, Hanover, NH 03755, USA

[6] Department of Astronomy, The University of Texas at Austin, Austin, TX 78712, USA

[7] Department of Physics and Astronomy, University of North Carolina, Chapel Hill, NC 27599, USA

Received 2022 February 25; revised 2022 April 1; accepted 2022 April 5; published 2022 May 24

Abstract

X-ray observations of low-mass stars in open clusters are critical to understanding the dependence of magnetic activity on stellar properties and their evolution. Praesepe and the Hyades, two of the nearest, most-studied open clusters, are among the best available laboratories for examining the dependence of magnetic activity on rotation for stars with masses $\lesssim 1\ M_\odot$. We present an updated study of the rotation–X-ray activity relation in the two clusters. We updated membership catalogs that combine pre-Gaia catalogs with new catalogs based on Gaia Data Release 2. The resulting catalogs are the most inclusive ones for both clusters: 1739 Praesepe and 1315 Hyades stars. We collected X-ray detections for cluster members, for which we analyzed, re-analyzed, or collated data from ROSAT, the Chandra X-ray Observatory, the Neil Gehrels Swift Observatory, and XMM-Newton. We have detections for 326 Praesepe and 462 Hyades members, of which 273 and 164, respectively, have rotation periods—an increase of 6× relative to what was previously available. We find that at ≈700 Myr, only M dwarfs remain saturated in X-rays, with only tentative evidence for supersaturation. We also find a tight relation between the Rossby number and fractional X-ray luminosity L_X/L_{bol} in unsaturated single members, suggesting a power-law index between −3.2 and −3.9. Lastly, we find no difference in the coronal parameters between binary and single members. These results provide essential insight into the relative efficiency of magnetic heating of the stars' atmospheres, thereby informing the development of robust age-rotation-activity relations.

Unified Astronomy Thesaurus concepts: Late-type stars (906); Stellar activity (1580); Open star clusters (1160); Stellar rotation (1629); X-ray point sources (1270); Binary stars (154)

Supporting material: figure sets, machine-readable tables

1. Introduction

In the interiors of low-mass stars (late-F dwarfs and later types), rotational shear at the tachocline, the boundary between the radiative and convective zones, is thought to power a dynamo (Parker 1993; Charbonneau 2014). This dynamo generates magnetic field that rises to the stellar surface where a fraction of the magnetic energy is dissipated and heats the corona to the $\gtrsim 10^6$ K temperatures required to produce thermal X-rays. Observations of GKM dwarfs with the Einstein Observatory found that their X-ray luminosity (L_X) is proportional to their rotational velocity, confirming this connection between L_X and rotation (Pallavicini et al. 1981; Pizzolato et al. 2003). Subsequent measurements of L_X, generally expressed as a fraction of the bolometric luminosity, L_X/L_{bol}, to remove the mass dependence, have shown that L_X/L_{bol} increases as the stellar rotation period (P_{rot}) decreases. This relation was refined by Noyes et al. (1984), who examined chromospheric fluxes in terms of the Rossby number, $R_o = P_{rot}/\tau$, where τ is the convective turnover time. L_X/L_{bol} then has a power-law dependence on R_o such that $L_X/L_{bol} \propto R_o^{\beta}$, with $\beta \approx -2$ (e.g., Randich 2000; Wright et al. 2011; Núñez et al. 2015; Thiemann et al. 2020). However, this holds only up to some threshold R_o, below which L_X/L_{bol} is ≈constant. For faster rotators, magnetic activity is saturated, i.e., it no longer depends on rotation speed (e.g., Stauffer et al. 1994; Pizzolato et al. 2003; Wright et al. 2011; Núñez et al. 2015).

The cause(s) of the saturation of X-ray activity are not well established, though several competing hypotheses have been formulated. A fundamental challenge is determining whether saturation is caused by changes in the dynamo efficiency, or is instead a consequence of fast rotation. The former could result in saturation of the dynamo (e.g., Gilman 1983; Blackman & Thomas 2015), although this is contradicted by observations that not all activity indicators appear to saturate, and that different indicators can saturate at different R_o (e.g., Cardini & Cassatella 2007; Mamajek & Hillenbrand 2008; Marsden et al. 2009). The latter could suggest that saturation instead occurs in the coronal filling factor (Vilhu 1984), although here again, the observational evidence is not strong, as studies have found that the coronal filling factor can be small in saturated X-ray emitters (e.g., Testa et al. 2004). Very rapid rotation could also cause coronal loops to become unstable due to the centrifugal force, a situation known as coronal stripping, as a result of the Keplerian corotation radius getting close to the stellar surface

---

[8] NSF MPS-Ascend Postdoctoral Research Fellow.

(Jardine & Unruh 1999). Other work has explored additional potential explanations, including changes in the underlying dynamo mechanism (from a convective dynamo to an interface dynamo; see Barnes 2003a, 2003b).

Meanwhile, some studies have also found that, in the fastest rotators, X-ray activity decreases relative to the saturation level, a phenomenon known as supersaturation (Randich et al. 1996). These authors found a decrease in L_X/L_{bol} for the fastest rotators ($v \sin i > 100$ km s^{-1}) in the ≈60 Myr-old open cluster α Persei. Subsequent studies have claimed to observe supersaturation in FGK dwarfs (Stauffer et al. 1997; Jeffries et al. 2011; Argiroffi et al. 2016), K dwarfs (Thiemann et al. 2020), M dwarfs, and ultracool dwarfs (Alexander & Preibisch 2012; Cook et al. 2014).

Supersaturation is even less well understood than saturation. James et al. (2000) and Jardine (2004) proposed that coronal stripping would explain both saturation and supersaturation, while Stępień et al. (2001) argued that supersaturation is caused by a decrease in the filling factor due to the poleward migration of active regions in very fast rotators. Wright et al. (2011) assembled a sample of 824 stars to study the dependence of L_X on R_o and found that their data favored the Stępień et al. (2001) hypothesis, even though the Keplerian corotation radius and the excess polar updraft were both better predictors of L_X/L_{bol} than either P_{rot} or R_o for their supersaturated stars. However, supersaturation does not appear to occur for chromospheric activity (e.g., Marsden et al. 2009; Jackson & Jeffries 2010), which argues against it being due to e.g., the migration of active regions, and favors the coronal-stripping explanation.

Further complicating our understanding of the coronal rotation-activity relation is the posited transition from a solar-type $\alpha\Omega$ dynamo in stars with a radiative core and a convective outer layer to a turbulent or α^2 dynamo in fully convective M dwarfs. Wright & Drake (2016) and Wright et al. (2018) found that fully convective M dwarfs follow the same L_X/L_{bol}–R_o relation as their partly convective counterparts, suggesting that fully and partly convective stars have very similar dynamos, driven mostly by the interaction of rotation and turbulent convection. This conclusion impugns the relevance of the shear at the tachocline in driving the magnetic dynamo in partly convective stars.

Studies of the dependence of L_X/L_{bol} on rotation have mostly focused on mixed-aged samples of open cluster and/or of field stars, where age effects are difficult to quantify (e.g., Randich et al. 2000; Wright et al. 2011, 2018; Thiemann et al. 2020). Other studies have instead focused on the single-aged populations in the handful of open clusters currently observable with X-ray telescopes,[9] where the number of detected stars is generally small (e.g., Douglas et al. 2014; Núñez et al. 2015, 2017). There is a clear need for more data before we can reach a consensus view on the age-dependence of the rotation–coronal activity relation or on the reason(s) for saturation and supersaturation.

The approximately coeval Praesepe and Hyades clusters, each about 700 Myr old, are the oldest open clusters within 250 pc, and thus the oldest accessible ensembles of low-mass stars with a well-constrained age.[10] Fully characterizing rotation and activity for the low-mass members of these two clusters is therefore critical to constraining the age-rotation-activity relation, particularly as Praesepe and the Hyades serve as a bridge of knowledge between younger cluster stars and their older field-age cousins.

This paper is the fourth in a series focused on Praesepe and the Hyades. In (Agüeros et al. 2011, Paper I), we presented P_{rot} for 40 Praesepe members measured using Palomar Transient Factory (PTF; Law et al. 2009; Rau et al. 2009) light curves. In (Douglas et al. 2014, Paper II), we combined literature P_{rot} and X-ray data with new and archival optical spectra for members of both clusters to show that L_X and Hα emission, a proxy for chromospheric activity, depend differently on R_o. In (Kraus et al. 2017, Paper III), we characterized a newly discovered eclipsing binary in Praesepe. Parallel to this paper series, in (Douglas et al. 2016, 2017, hereafter D16 and D17) we added 48 new P_{rot} for Hyades members and 677 for Praesepe members from an analysis of K2 (Howell et al. 2014) photometry. And in Rampalli et al. (2021) we used two additional K2 campaigns to complete the census of rotation in Praesepe, measuring new P_{rot} for 220 stars and bringing the total number of P_{rot} for the cluster to 1013.

We begin below by revisiting the membership catalogs for the two clusters in light of the information provided by the Gaia data, and particularly by its Data Release 2 (GDR2; Gaia Collaboration et al. 2018a), in Section 2. We also discuss the P_{rot} available for both clusters, using these to calculate R_o for their members, as well as binary information for stars in the two clusters. In Section 3 we present our analysis of the extensive set of X-ray observations we have assembled for Praesepe and the Hyades from the Röntgen Satellite (ROSAT), the Chandra X-ray Observatory (Chandra), the Neil Gehrels Swift Observatory (Swift), and the X-ray Multi-Mirror Mission Newton (XMM). We derive several stellar parameters for cluster stars in Section 4. We present our results in Section 5 and conclude in Section 6.

2. Constructing Our Membership Catalogs

2.1. Legacy Membership Catalogs

Douglas et al. (2014) and D17 based their Praesepe catalog on the cluster membership probabilities P_{mem} calculated by Kraus & Hillenbrand (2007). These P_{mem} were found for $>10^6$ sources in the field of view of Praesepe using photometric and astrometric data. D17 considered the Kraus & Hillenbrand (2007) 1130 stars with $P_{mem} \geqslant 50\%$ as bona fide cluster members. To these stars, D17 added 39 previously identified Praesepe members too bright to be included in the Kraus & Hillenbrand (2007) catalog, assigning these stars $P_{mem} = 100\%$. As a starting point, we took all stars from Kraus & Hillenbrand (2007) with $P_{mem} \geqslant 10\%$ to be potential Praesepe members; we also added the 39 additional stars from D17 as bona fide members.

As in D16, we adopted the Goldman et al. (2013) catalog for the Hyades and supplement it with members identified through analysis of Hipparcos data (Perryman et al. 1997). All but 13 Hyads identified through this analysis were also identified by Goldman et al. (2013). In Goldman et al. (2013), stars have discrete values for field contamination (100, 30, 17.5, or 1%). D16 adopted the invert of these values as P_{mem} and considered stars with $P_{mem} \geqslant 70\%$ (corresponding to contamination fraction $\leqslant 30\%$) as bona fide members. As a starting point, we took all stars in D16 with $P_{mem} > 0\%$ to be potential Hyades members.

---

[9] The small fields-of-view of the current flagship X-ray observatories are poorly matched to the size of nearby open clusters, while the low-mass members in more distant, smaller-on-the-sky clusters require excessive exposure times.

[10] Douglas et al. (2019) combined literature estimates for the age of Praesepe to assign the cluster an age of 670 ± 67 Myr, and used gyrochronology to determine that the Hyades is 57 Myr older, or 727 ± 75 Myr old.

Table 1
Praesepe and Hyades Membership Catalogs Considered in This Work

	# of Members	
Provenance	Praesepe	Hyades
Legacy Catalogs	1123	746
Cantat-Gaudin et al. (2018)	719	…
Gaia Collaboration et al. (2018b)	937	508
Lodieu et al. (2019a)	721	…
Lodieu et al. (2019b) [a]	…	556
Meingast & Alves (2019)	…	238
Röser et al. (2019)	…	976
Röser & Schilbach (2019)	1393	…
Ultracool Dwarfs[b]	12	21
Consolidated # of Members	1739	1315

Notes.
[a] We did not include the set of stars farther than 18 pc from the cluster center, as these authors considered this set to have a significant level of contamination.
[b] Late M dwarfs and brown dwarfs found in the literature. See Section 2.3.

2.2. *Gaia-based Membership Catalogs*

Successive Gaia data releases have transformed our view of the membership of stellar clusters. Table 1 lists the Gaia-based studies of Praesepe and the Hyades that we considered, in addition to our legacy catalogs, to produce our definitive membership catalogs, and the number of members included in each. Our starting assumption was that the Gaia-based catalogs are correct, in that they are likely to contain fewer contaminants than earlier catalogs—thanks in part to Gaia's higher spatial resolution—but are incomplete, in that Gaia data either lack five-parameter solutions or have poor fits for unresolved binaries (e.g., Belokurov et al. 2020). Gaia-based studies, therefore, exclude most potential binaries from published cluster catalogs.

To produce our updated catalogs, we first cross-matched our legacy catalogs against the GDR2-based catalogs using a $5''$ matching radius. To account for the large proper motions of Hyads, we also searched for GDR2 counterparts using a matching radius between $5''$ and $7''$ and found 17 additional matches; we inspected these visually using Aladin Sky Atlas.[11] We found two or more GDR2 stars within the matching radius of 161 Hyads and 80 Praesepe stars. We assumed the closest match to be the best match, except when the radial distances of the potential matches were too similar. In such instances, we guided our best match selection using GDR2 parallax, proper motion, and photometry for each potential match. We resolved ambiguous matches using this approach for 23 Hyads and 5 Praesepe stars. All in all, the median closest matching radius was $1\overset{''}{.}6$ for Hyads and $0\overset{''}{.}6$ for Praesepe stars.

Stars that appeared as members in our legacy catalogs and are included in any of the GDR2 catalogs in Table 1 form the bulk of our final catalogs. There are 746 Hyads and 1123 Praesepe stars in this category. If, however, a star was not in our legacy catalogs but is included as a member in any of the GDR2 catalogs, we added that star to our list of bona fide members for that cluster. In Praesepe, there are 292 such stars in the core, and 312 in the tidal tails. In the Hyades, the numbers are 143 and 405, respectively.

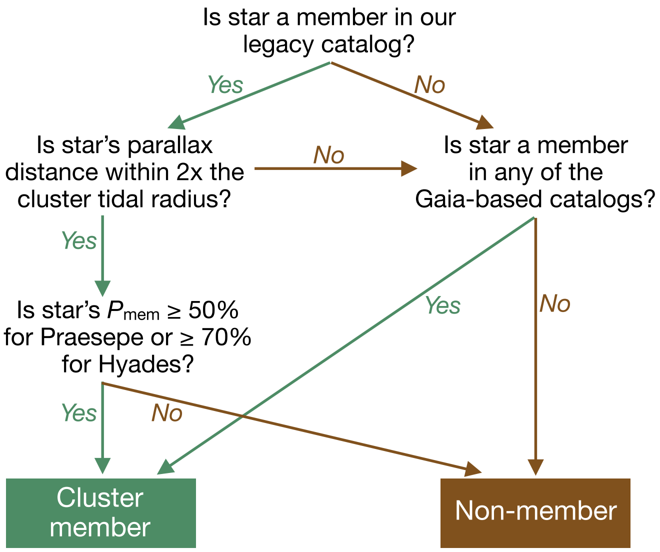

Figure 1. Decision process to consolidate our Praesepe and Hyades legacy catalogs (described in Section 2.1) with the GDR2-based catalogs listed in Table 1.

We then matched our catalog stars to Gaia Early Data Release 3 (GEDR3; Gaia Collaboration et al. 2021, see Section 2.4) to obtain GEDR3 photometry and GEDR3-based distances from Bailer-Jones et al. (2021). For stars without such distances, we found either parallax or distance calculations in the literature. For Hyades, we found 2 Hipparcos-based parallaxes in van Leeuwen et al. (2007), 51 PPMXL-based parallaxes in Röser et al. (2011), and one trigonometric parallax in Dittmann et al. (2014). We also found eight spectroscopic distances in Lodieu et al. (2014), one photometric distance in Robert et al. (2016), and two photometric distances in Schneider et al. (2017). For all other stars missing distances (68 Praesepe stars and five Hyads), we assigned them a distance equal to that of the cluster as a whole. To estimate the distance of each cluster as a whole, we calculated the median, 16th, and 84th percentiles of the Bailer-Jones et al. (2021) distances.[12] The resulting cluster distances are $183.2^{+11.1}_{-13.7}$ pc for Praesepe and $49.1^{+25.4}_{-7.7}$ pc for the Hyades; the 1σ distance errors were approximated as the mean of the 16th and 84th percentiles.

Figure 1 illustrates as a decision tree the steps described next to build our cluster catalogs. To start, we compared the one-dimensional parallax distance ($\pm 2\sigma$) of each star in our legacy catalogs to its cluster's center ± twice the tidal radius, which we took to be 11.5 pc for Praesepe (Kraus & Hillenbrand 2007) and 10 pc for Hyades (Röser et al. 2011). If the star is closer to or farther from us than these distances, indicating that it is beyond twice the tidal radius for its cluster, we categorized that star as a nonmember.

We then checked whether a star that was rejected as a nonmember in the step above is considered a member in any of the GDR2 catalogs. We assumed that such stars are bona fide members and therefore added them back in to our final catalogs.

Lastly, we rejected stars from our legacy catalogs that passed the above radial distance check but that have $P_{\rm mem}$ lower than the thresholds used in D16 and D17: 70% for Hyades and 50%

---

[11] We also tracked these 17 stars in our subsequent analysis. Ten of them have X-ray detections; none of which stand apart from their spectral type cohort in their X-ray measurements.

[12] We excluded the tidal tail stars cataloged for both clusters (Meingast & Alves 2019; Röser et al. 2019; Röser & Schilbach 2019) to calculate these cluster distances.

Table 2
Overview of Columns in the Praesepe and Hyades Membership Catalog

Column	Description
1	Name
2	2MASS designation
3	Gaia EDR3 designation
4, 5	R.A., Decl. for epoch J2000
6	Cluster to which the star belongs
7	Member in legacy catalog?
8	Member in Cantat-Gaudin et al. (2018)?
9	Member in Gaia Collaboration et al. (2018b)?
10	Member in Lodieu et al. (2019a)?
11	Member in Lodieu et al. (2019b)?
12	Member in Meingast & Alves (2019)?
13	Member in Röser & Schilbach (2019)?
14	Member in Röser et al. (2019)?
15	Ultracool dwarf in literature?
16, 17	Distance and 1σ uncertainty
18	Source of distance[a]
19, 20	K-band magnitude and 1σ uncertainty
21	Source of K magnitude[b]
22, 23	Gaia EDR3 G band magnitude and 1σ uncertainty
24	Source of G magnitude[c]
25	Gaia EDR3 $G_{\rm BP} - G_{\rm RP}$
26	Binary flag: (0) no binary flag; (1) candidate binary; (2) confirmed binary
27	Gaia EDR3 RUWE
28	Rotation period $P_{\rm rot}$
29, 30	X-ray energy flux $f_{\rm X}$ (0.1–2.4 keV) and 1σ uncertainty
31	Stellar mass
32	Convective turnover time τ
33, 34	$L_{\rm bol}$ and 1σ uncertainty

Notes.
[a] BJ: Bailer-Jones et al. (2021); C: Cluster distance; D: Dittmann et al. (2014); L: Lodieu et al. (2014); P: Pérez-Garrido et al. (2018); R11: Röser et al. (2011); R16: Robert et al. (2016); S: Schneider et al. (2017); vL: van Leeuwen et al. (2007); Z: Zhang et al. (2010).
[b] 2M: 2MASS; B: Boudreault et al. (2010); G: Derived from GEDR3 photometry; UL: UKIDSS LAS; UG: UKIDSS GCS.
[c] 2M: Derived from 2MASS photometry; G: GEDR3.

(This table is available in its entirety in machine-readable form.)

for Praesepe, respectively (see Section 2.1). As these stars were not present in any of the GDR2 catalogs and they have low $P_{\rm mem}$ in the legacy catalogs, we consider them to have a high probability of being field contaminants.

Table 2 includes our consolidated catalog of Praesepe and Hyades stars. Column 7 of Table 2 specifies if a star is a member in our legacy catalogs, and Columns 8–14 specify if a star is considered a cluster member in each of the GDR2 catalogs. Our resulting catalogs include 1727 Praesepe members and 1294 Hyads. To these, we add ultracool dwarfs from the literature, as we explain next.

2.3. Ultra-cool Dwarfs

To our consolidated cluster catalogs, we added ultracool dwarfs that were not already included in our legacy catalogs or in the GDR2-based catalogs. These are primarily late M and early-to-mid L dwarfs. We found twelve such Praesepe stars in the literature: one M9 and four L0 type dwarfs from Boudreault et al. (2010), one L0 found by Zhang et al. (2010), and four late M and two early-L dwarfs from Manjavacas et al. (2020). To the Hyades catalog we added 21 objects: two late M and four early-L dwarfs cataloged by Lodieu et al. (2014), one L3 found by Robert et al. (2016), two mid L found by Schneider et al. (2017), and three late M and nine L dwarfs found by Pérez-Garrido et al. (2018). Column 15 of Table 2 indicates whether a cluster star is an ultracool dwarf from the literature.

Only eight ultracool dwarfs (one Praesepe and seven Hyads) have Bailer-Jones et al. (2021) distances. For the others, we adopted either the distances from the literature—which was the case for one Praesepe and 14 Hyads—or the cluster distance as a whole (see Section 2.2).

The final tallies in our cluster catalogs are 1739 Praesepe stars and 1315 Hyads.

2.4. Photometry

As mentioned in Section 2.2, we matched our final catalog from Sections 2.2 and 2.3 against GEDR3 using a 3″ matching radius for stars in both clusters. When we found more than one GEDR3 star within the matching radius, we compared the G magnitudes, when available, to determine the better match. In most cases, the closest match was the best match.

We obtained GEDR3 magnitudes for 2684 members of the two clusters (1732 for Praesepe, 1304 for the Hyades), ranging from $G = 2.7$ to 21.1 mag. For seven ultracool dwarf Praesepe members and eleven ultracool dwarf Hyads lacking a GEDR3 counterpart, we derived G magnitudes from Two Micron All-Sky Survey (2MASS; Skrutskie et al. 2006) J and K magnitudes using the transformations given by Riello et al. (2021). These ultracool dwarfs cover the magnitude range $14.5 < K < 17.1$, and the derived G magnitudes are in the range $19.6 < G < 25.2$.

We also collected good quality (PH_QUAL A, B, or C) 2MASS K magnitudes for 1669 Praesepe and 1274 Hyades members. The resulting coverage is $1.5 < K < 15.7$ mag. For the 111 Praesepe and Hyades stars lacking a good quality 2MASS K, we searched for K photometry from the United Kingdom InfraRed Telescope (UKIRT) Infrared Deep Sky Survey (UKIDSS; Lawrence et al. 2007) data release 9, both from the Galaxy Clusters Survey (GCS) and Large Area Survey (LAS). We found UKIDSS K photometry for 41 additional Praesepe members and nine Hyads, covering the magnitude range $9.8 < K < 18.8$.

There are nine Praesepe stars lacking good quality 2MASS/UKIDSS K photometry. For these stars, we derived K magnitudes from GEDR3 G and $(G_{\rm BP} - G_{\rm RP})$ color using the transformations given in Riello et al. (2021). There are also 20 Praesepe stars unmatched in 2MASS/UKIDSS. Ten of these are newly identified white dwarfs in the GDR2 catalogs, and five others are secondary stars in binaries unresolved by 2MASS/UKIDSS. Except for one of the white dwarfs and three of the secondary stars—all lacking a $(G_{\rm BP} - G_{\rm RP})$ color, we derived their K magnitudes using the same transformations as above. The remaining five unmatched stars are ultracool dwarfs, for which we adopt the K magnitudes measured in Boudreault et al. (2010).

In the Hyades, there are 27 stars lacking good quality 2MASS/UKIDSS K photometry. We derived their K magnitudes using the transformations in Riello et al. (2021) mentioned above. There are also five Hyads unmatched in 2MASS/UKIDSS. Three of these are newly identified white dwarfs in the GDR2 catalogs, and two are secondary stars in binaries unresolved by 2MASS/UKIDSS. We derived their K magnitudes using the same transformations as above. The magnitude range of all derived K magnitudes is $1.0 < K < 19.7$. Column 21 of Table 2 identifies the source of the K magnitude for each star.

All in all, we have G photometry for all stars in our catalogs, and K photometry for all but four Praesepe stars. The combined photometry covers the color range $-0.9 < (G-K) < 10.4$ mag. We calculated absolute G magnitudes (M_G) for our cluster stars using the distances we adopted for each, and an extinction correction for the Gaia G band. We obtained the latter by first calculating the total absorption in V (A_V) using the extinction tables by Schlafly & Finkbeiner (2011) assuming $R_V = 3.1$ and adopting a reddening of $E(B-V) = 0.035$ for Praesepe (Douglas et al. 2019) and 0.001 for the Hyades (Taylor 2006). We then obtained the total absorption in G (A_G) using $A_G/A_V = 0.789$ (Wang & Chen 2019). The left panels of Figure 2 show the M_G—$(G-K)$ color–magnitude diagram (CMD), and the right panels, the M_G—$(G_{\rm BP}-G_{\rm RP})$ CMD[13] for both clusters.

2.5. Rotation Periods

The most up-to-date catalogs of rotation periods for the two clusters are those of Rampalli et al. (2021) for Praesepe and Douglas et al. (2019) for the Hyades. Both of these catalogs supplement ground-based $P_{\rm rot}$ measurements with large numbers of $P_{\rm rot}$ obtained from the five K2 campaigns dedicated to the two clusters (C5, C16, and C18 to Praesepe, and C4 and C13 to the Hyades). In total, we have $P_{\rm rot}$ measurements for 1052 Praesepe members and 233 Hyads. Column 28 in Table 2 includes these $P_{\rm rot}$ values.

2.6. Binary Flags

To identify binaries and multiple systems in the two clusters, we relied on the binary flags from several previous studies. D16 and D17 obtained and tabulated binary flags for members of Hyades and Praesepe, respectively. Douglas et al. (2019) updated and complemented those flags and reported the following individual flags: visual identification, UVW kinematic deviations (for Hyades only), vertical distance from the main sequence on a Gaia CMD, multiple periodicity from K2 periodograms, GDR2 radial velocity and proper motion deviations, high GDR2 astrometric excess noise ($\epsilon_i > 1$), and confirmed binarity from the literature. Rampalli et al. (2021) further updated these flags for Praesepe and replaced the $\epsilon_i > 1$ flag with GEDR3's re-normalized unit weight error (RUWE) > 1.2 to identify likely unresolved binaries (see binary indicators in their Table 4).

In our catalog, we consider as *candidate* binaries (Binary Flag = 1) stars having at least one of the kinematics, CMD distance, radial velocity, proper motion, or multiple periodicity flags. We consider as *confirmed* binaries (Binary Flag = 2) those confirmed in the literature. However, we ignore the ϵ_i and the RUWE flags in Douglas et al. (2019) and Rampalli et al. (2021), respectively, as we implement our own approach to using the most recent GEDR3 spurious astrometry indicators (see our RUWE treatment in the next paragraph). Also, we found ten Praesepe stars and seven Hyads for which GEDR3 resolved two point sources and 2MASS only one. We assigned Binary Flag = 1 to these 17 stars. All in all, we have 456 candidate and 82 confirmed binaries in Praesepe and 60 candidate and 238 confirmed binaries in Hyades. Figure 3 shows the same CMDs as in Figure 2, this time highlighting with orange crosses candidate/confirmed binaries. Column 26 of Table 2 includes our binary flag for each star.

Lastly, we collected RUWE values for our stars.[14] The RUWE is a goodness-of-fit measure of the single-star model fit to the source's astrometry. If a star is an unresolved binary and its center of light deviates from the assumed single-star model, its RUWE will deviate significantly from 1.0 (e.g., Jorissen 2019; Belokurov et al. 2020). Gaia cannot resolve separations $\lesssim 0\farcs7$ (Ziegler et al. 2018), which corresponds to a semimajor axis $a \approx 35$ au at the typical Hyad distance and ≈ 130 au at the typical Praesepe star distance. Therefore, most stars in our catalogs with high RUWE are likely to be "intermediate" binaries, i.e., with small enough separation ($0.1 \lesssim a \lesssim 80$ au) for the binary components to have affected each other's protoplanetary disks in the first 10 Myr (Rebull et al. 2006; Meibom et al. 2007; Kraus et al. 2016; Messina et al. 2017, S. T. Douglas et al. 2022, in preparation). They are unlikely to be tight, tidally interacting binaries ($a \lesssim 0.1$ au) because their center of light will deviate minimally from the assumed single-star model ($a = 0.1$ au corresponds to $\delta\theta \approx 2$ mas at the typical Hyad distance and ≈ 0.5 mas at the typical Praesepe star distance), thus only negligibly deviating RUWE from 1.0.

Typically, stars with RUWE > 1.4 are considered to have high probability of being unresolved binaries (e.g., Deacon & Kraus 2020; Ziegler et al. 2020; Kervella et al. 2022), although some studies have used a more conservative >1.2 threshold to identify potential binaries (e.g., Pearce et al. 2020). We use RUWE > 1.4 to determine which stars with Binary Flag = 0 (i.e., assumed to be single) are potentially unresolved binaries. However, we do not necessarily exclude them from the sample of single stars in our analysis, because we do not have any additional information on their potential binarity. Column 27 of Table 2 includes the RUWE for each star. In Praesepe, 52 (4%) stars with Binary Flag = 0 and 129 (24%) with Binary Flag > 0 have RUWE > 1.4. For Hyades, the numbers are 152 (15%) and 131 (44%), respectively.

3. X-Ray Data

Over the past few decades, Praesepe and the Hyades have been regularly targeted by X-ray missions, and members of both clusters have also been detected serendipitously. We collected data from ROSAT, Chandra, XMM-Newton, and Swift. In some cases this required extracting sources from the X-ray observations ourselves. In others, we relied on previously compiled lists of X-ray detections, typically serendipitous source catalogs, which are constructed from automated processing of archival pointings. We homogenized these data to build a complete and uniform set of X-ray detections. To achieve this, our approach was to use the reported count rates and our own energy conversion factors (ECF; see Section 4.3) to obtain unabsorbed X-ray energy fluxes, $f_{\rm X}$, in the 0.1–2.4 keV energy band.[15] We then

---

[13] We collected $(G_{\rm BP}-G_{\rm RP})$ for 1724 Praesepe and 1301 Hyades stars, although we do not use this Gaia color in our analysis.

[14] Both ϵ_i and RUWE have their pros and cons in identifying spurious Gaia astrometry; we opted to use only RUWE by virtue of its more sound and guaranteed distribution (with peak at 1.0) across the full color–magnitude range of Gaia (see discussions in Belokurov et al. 2020; Penoyre et al. 2020)

[15] We chose the most restrictive energy bandpass out of the four X-ray observatories to homogenize our data, which happens to be the ROSAT bandpass.

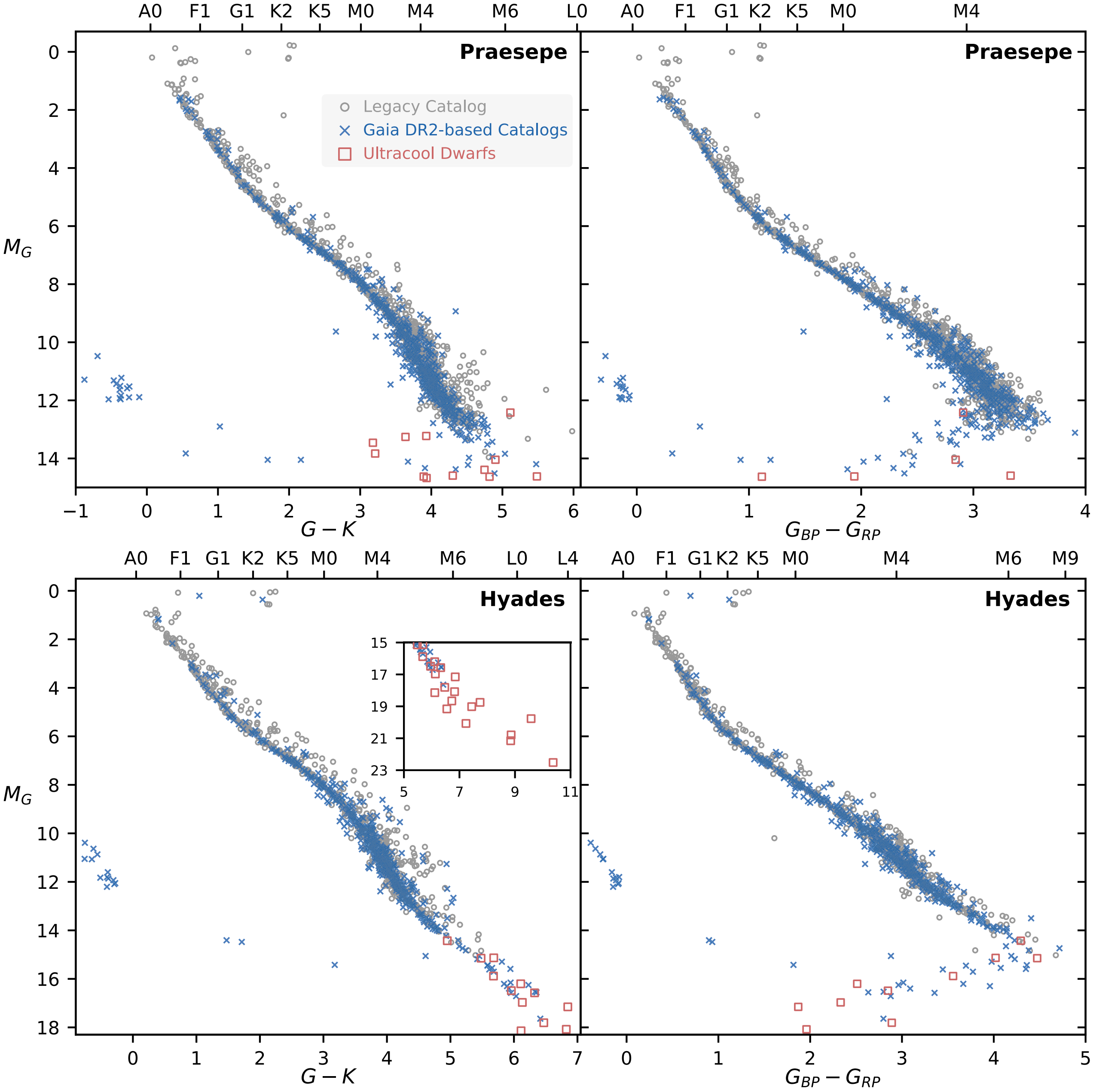

Figure 2. CMDs for Praesepe (top panels) and Hyades (bottom). The left column combines GEDR3 and either 2MASS, UKIDSS, or GEDR3-derived K photometry to produce a $(G-K)$ color. The right column uses the $(G_{\mathrm{BP}}-G_{\mathrm{RP}})$ color from GEDR3. Our full catalog consists of stars from our legacy catalog (gray circles, see Section 2.1), Gaia DR2-based studies of cluster membership (blue × symbols, see Section 2.2), and ultracool dwarfs from the literature (red squares, see Section 2.3). The bottom left panel includes an inset to show the full red end of the main sequence for Hyades in $(G-K)$ color. We have a total of 1739 Praesepe members and 1315 Hyades members in our full catalog.

converted f_X to L_X by using our adopted individual distances. For Chandra, XMM, or Swift sources with enough X-ray counts, we performed spectral analysis to extract unabsorbed f_X as well as coronal temperature, coronal metal abundance, and, in some cases, neutral hydrogen column density along the line of sight.

In the few instances in which the count rates were not reported, namely, some ROSAT-based studies, we worked backwards from the reported L_X, distance, and ECF to estimate the count rates and then applied the procedure described above to obtain our own f_X and L_X values. Figure 4 illustrates the number of Praesepe and Hyades stars detected with at least one of the X-ray observatories.

Our full list of X-ray detections for Praesepe and Hyades stars is in Table 3. If a star had more than one X-ray detection, we calculated the error-weighted average of the f_X values and adopted it as the bona fide f_X for that star. Columns 29 and 30 of Table 2 include the f_X and 1σ uncertainty for each cluster star with at least one X-ray detection. In total, we have 504 individual X-ray detections for 326 Praesepe stars (two of which are ultracool dwarfs), and 603 for 464 Hyads (three ultracool dwarfs). Only 3% of X-ray detections have questionable quality (see Column 28 in Table 3).

In the next subsections, we explain in detail the X-ray source detection and photometric extraction we performed with data from each X-ray observatory.

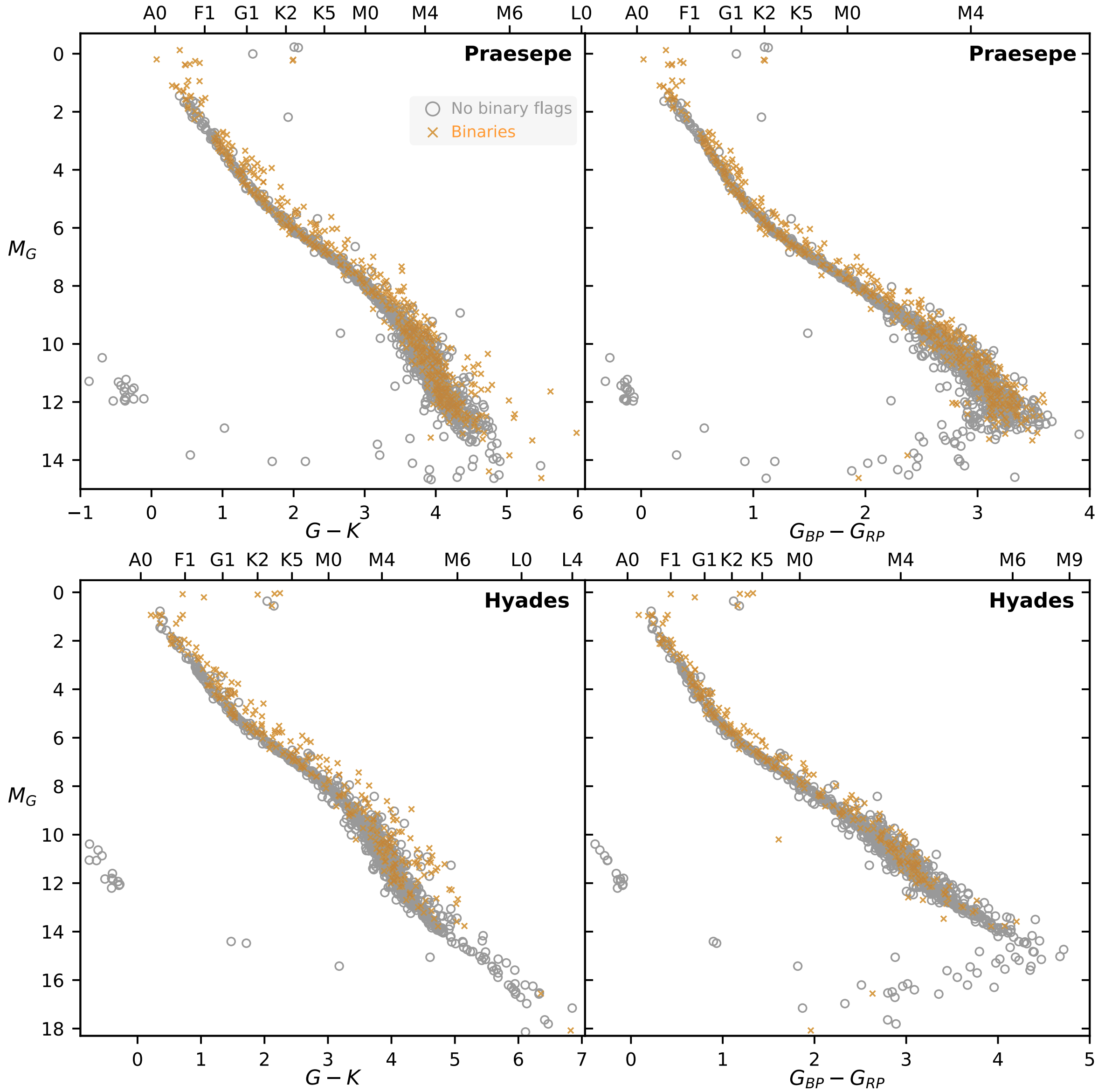

Figure 3. Same as in Figure 2, but this time indicating stars with no binary flags with gray circles, and candidate/confirmed binaries with orange crosses. Candidate/confirmed binaries constitute 31% of our Praesepe catalog and 23% of our Hyades catalog.

3.1. ROSAT Observations

3.1.1. ROSAT Sources from the Publicly Released Catalogs

We searched for X-ray counterparts to our cluster stars in the latest versions of the three publicly released ROSAT catalogs: the Second ROSAT Source Catalog of Pointed Observations with the Position Sensitive Proportional Counters (PSPC) catalog (2RXP; ROSAT Consortium 2000), the Second ROSAT All-Sky Survey (RASS) catalog (2RXS, Boller et al. 2016), and the ROSAT High-resolution Imager Pointed Observations catalog (1RXH; ROSAT Scientific Team 2000). We cross-matched these ROSAT catalogs and our cluster catalogs using a 50″ radius; this value was chosen to be large enough to account for the large ROSAT positional errors. To estimate the number of likely false matches, we shifted the X-ray source positions in steps of 50″ out to 10′ in all directions and re-matched them to the cluster catalogs using the same 50″ radius used before. All resulting matches are assumed to be false. We found that the median number of false matches is 30 (≈8% of our matched ROSAT sources) with a median offset of 34″. In our final ROSAT-cluster catalogs matches, we consider those with radii >30″ in Praesepe and >40″ in Hyades to be likely false matches, and we exclude those from our X-ray analysis, although we still include them in our consolidated catalog of X-ray sources, with a "likely false match" flag (Quality Flag = "x"; Column 28 of Table 3).

From the ROSAT catalogs, we obtained count rates and some other information about the X-ray point sources, such as hardness ratios, detection likelihoods, and variability flags, when available (see Table 3). We used the published count rates, our own ECFs (see Section 4.3), and our adopted individual distances to calculate f_X and L_X in the 0.1–2.4 keV energy band.

In the 2RXP catalog, we found X-ray counterparts for 78 Praesepe stars and 56 Hyads. Five Praesepe stars have a matching radius >30″, and we flagged these matches as likely false matches. All 56 Hyads, on the other hand, have a matching radius <20″. We also found six additional Praesepe

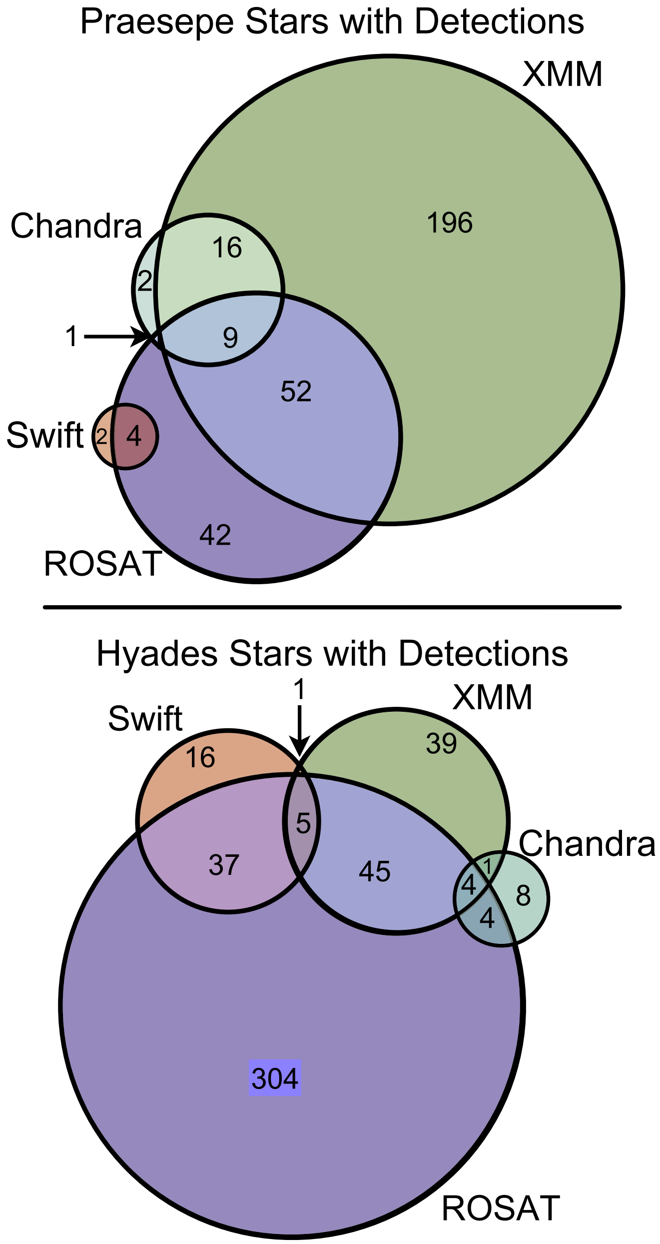

Figure 4. Venn diagrams illustrating the number of Praesepe (top panel) and Hyades (bottom panel) stars detected in X-rays with the four X-ray observatories. In our Praesepe catalog, 19% of stars are detected in X-rays. In our Hyades catalog, the number is 35%.

and 90 Hyades stars with X-ray counterparts at large $(>20')$ offset angles from the instrument aimpoint. For these X-ray sources, 2RXP did not present count rate uncertainties, and so we opted to ignore these X-ray sources. Also, one of the sources matched to a Praesepe star has a source extent maximum likelihood higher than its source detection maximum likelihood; we therefore flag this source as a likely extended source in Table 3. Lastly, we found six additional 2RXP X-ray sources with ambiguous matches to stars in our catalogs. In these cases, each X-ray source had either two Praesepe stars within a $15''$ radius or two Hyads within a $40''$ radius roughly equidistant, and we opted to ignore these X-ray sources, as it was not possible to determine the true optical source of the X-ray detection.

Table 3
Overview of Columns in the X-ray Source Catalog

Column	Description
1	External catalog source ID
2	Provenance of X-ray information[a]
3	IAU Name
4	Observation ID
5	Instrument
6, 7	R.A., Decl. for epoch J2000
8	X-ray positional uncertainty
9	Off-axis angle θ
10	Detection likelihood L[b]
11	Net counts in the broad band
12, 13	Net count rate and 1σ uncertainty in broad band
14, 15	Net count rate and 1σ uncertainty in soft band
16, 17	Net count rate and 1σ uncertainty in hard band
18–20	Definition of broad, soft, and hard bands
21	Hardness ratio: (hard band − soft band) / (hard band + soft band)
22	Exposure time
23	Variability flag: (0) no evidence for variability; (1) possibly variable; (2) definitely variable
24, 25	Unabsorbed energy flux and 1σ uncertainty in the 0.1–2.4 keV band
26	Source of energy flux: (ECF) from applying ECF; (SpecFit) from spectral fitting
27	X-ray flare removed?
28	Quality Flag[c]
29	Name of the optical counterpart
30	Separation between X-ray source and optical counterpart

Notes.

[a] 1RXH; 2RXP; 2RXS; CSC; CIAO: Reduction of Chandra observation with CIAO; R95: Randich & Schmitt (1995); S01: Stelzer & Neuhäuser (2001); S95: Stern et al. (1995); SAS: Reduction of XMM observations with SAS; Swift.

[b] For CIAO sources, it is the source significance; for all others, it is the maximum likelihood.

[c] m: likely mismatch to optical counterpart; x: likely extended source.

(This table is available in its entirety in machine-readable form.)

In the 2RXS catalog, we found X-ray counterparts for nine Praesepe stars and 312 Hyads. One Praesepe star has a matching radius $>30''$, and 19 Hyads have a matching radius $>40''$. We flagged these 20 matches as likely false matches. Furthermore, five of the Praesepe matches and 35 of the Hyades matches were also found in the 2RXP catalog, and we opted to adopt the X-ray information for these 40 sources from the 2RXP catalog instead.[16] Lastly, we found nine additional 2RXS X-ray sources with ambiguous matches to Hyads. In each case, the X-ray source had two roughly equidistant Hyads within a $30''$ radius, and we opted to ignore these X-ray sources, as it was not possible to determine the true optical source of the X-ray detection. All in all, we include 2RXS sources for four Praesepe stars and 277 Hyads, and their X-ray information is included in Table 3.

Lastly, in the 1RXH catalog, we found X-ray counterparts for one Praesepe star and 22 Hyads. All matches to 1RXH have

---

[16] The 2RXP catalog was curated for point sources by both automatic algorithms and detailed visual inspection. As such, we assume 2RXP to be a more reliable source of X-ray information than 2RXS.

a matching radius <15″, and none of them were found in the 2RXP or the 2RXS catalogs.

3.1.2. ROSAT Sources from Independent Studies

To complement the ROSAT X-ray sources we found in the publicly released ROSAT catalogs, we also searched for X-ray counterparts from ROSAT studies of Praesepe and Hyades in the literature. Such studies sometimes included sources that were otherwise rejected by the automatic pipelines of the ROSAT catalogs, but that were otherwise acceptable knowing the nature of the X-ray emission (i.e., hot plasma from the atmospheres of low-mass stars). We describe below the individual ROSAT studies and the data we used from each one, which is included in Table 3.

Stelzer & Neuhäuser (2001) used PSPC data publicly available as of 1998 October and analyzed by Stelzer et al. (2000) to report 0.1–2.0 keV quiescent[17] L_X and hardness ratio (HR) values for 181 Hyads in our catalog. We used L_X and HR values published by Stelzer & Neuhäuser (2001) and the distances adopted by these authors (from Hipparcos when available; otherwise, 46 pc) to calculate the corresponding X-ray count rates, using the formula $\mathrm{ECF} = (8.31 + 5.30 \times \mathrm{HR}) \times 10^{-12}\,\mathrm{erg\,cm^{-2}\,count^{-1}}$, as adopted in their work.

Of the 181 X-ray sources in Stelzer & Neuhäuser (2001), 126 are also in the ROSAT catalogs, and we opted to adopt the X-ray information for these 126 sources from the ROSAT catalogs instead. Therefore, we used X-ray information for only 55 Hyads from the Stelzer & Neuhäuser (2001) catalog.

Stern et al. (1995) used data from the RASS (Voges et al. 1999) to extract X-ray point sources and match them to an optical catalog of 440 Hyads put together by these authors. They found 187 matches to cluster stars and 24 matches to stars they considered nonmembers. For the former, they only published L_X values in the 0.1–1.8 keV band, which were calculated assuming a distance of 45 pc and an ECF of $6.0 \times 10^{-12}\,\mathrm{erg\,cm^{-2}\,count^{-1}}$. For the latter, they instead published count rates in the 0.1–1.8 keV band. We converted the published L_X for cluster stars back into count rates.

Of the 211 X-ray sources in Stern et al. (1995), 174 are also in the ROSAT catalogs, and we opted to adopt the X-ray information for these 174 sources from the ROSAT catalogs instead. Seven additional sources are also in the Stelzer & Neuhäuser (2001) catalog, and we opted to adopt the X-ray information for these seven sources from the latter catalog instead. Furthermore, we found 18 of their sources to be nonmembers. Finally, we found five sources with ambiguous optical counterparts, and we opted to ignore those, as it was not possible to determine the true optical counterparts to these five X-ray sources. In summary, we used X-ray information for only seven Hyads from the Stern et al. (1995) catalog.

Randich & Schmitt (1995) surveyed Praesepe using the PSPC instrument aboard ROSAT. These authors obtained 42 0.4–2.0 ks fields in a raster scan pattern over two years of observations, detecting 68 stars in the Klein Wassink (1927); Jones & Cudworth (1983), and Jones & Stauffer (1991) Praesepe catalogs. For these 68 stars, Randich & Schmitt (1995) published X-ray count rates in the 0.4–2.0 keV band.

Of the 68 X-ray sources in Randich & Schmitt (1995), 39 are in the ROSAT catalogs, and we opted to adopt the X-ray information for these 39 sources from the ROSAT catalogs instead. We also found two of their sources to be nonmembers. Finally, we found one source with an ambiguous optical counterpart, and we opted to ignore this source, as it was not possible to determine its true optical counterpart. Therefore, we used X-ray information for only 26 Praesepe stars from the Randich & Schmitt (1995) catalog.

Reid et al. (1995) published the results of three 30–40 ks PSPC observations offset by 3°–4° from the Hyades cluster center. These authors detected 20 Hyads, 19 of which are also considered members in our updated membership catalog. However, we did not use any X-ray information from this X-ray catalog. Nine of their sources are in the ROSAT catalogs, and we opted to adopt the X-ray information for these sources from the ROSAT catalogs instead. The remaining ten X-ray sources are all present in the Stelzer & Neuhäuser (2001) catalog, and we opted to adopt the X-ray information for these sources from the latter catalog.

3.2. Chandra Observations

3.2.1. Data from the Chandra Source Catalog

We searched for X-ray counterparts to our cluster stars in the latest version of the Chandra Source Catalog (CSC 2.0, Evans et al. 2020a). We cross-matched the CSC and our cluster catalogs using a 15″ radius. We found CSC counterparts to ten Praesepe stars and nine Hyads, all have a matching radius <8″. Eleven of these CSC sources were observed with an ACIS-I chip, six with an ACIS-S chip, and two with the high-resolution camera instrument. In Figure 5 we draw in blue the ACIS footprints of archival observations that include sources matched to Praesepe stars.[18]

Like with ROSAT (see Section 3.1.1), we estimated the number of likely false matches by shifting the X-ray source positions in steps of 25″ out to 3′ in all directions and rematched them to the cluster catalogs using the same 15″ radius used before. All resulting matches are assumed to be false. We found that the median number of false matches is 2 (≈10% of our matched CSC sources) with a median offset of 10″. As such, we consider all our final CSC-cluster catalogs matches to be true matches.

From the CSC, we obtained count rates in the 0.5–2.0 (soft), 2.0–7.0 (hard), and 0.5–7.0 (broad) keV bands, plus some other information about the X-ray point sources, such as detection likelihoods, and variability flags (see Table 3). We used the published count rates, our own ECFs (see Section 4.3), and our adopted individual distances to calculate f_X and L_X in the 0.1–2.4 keV band. Information about the original Chandra observations that collected the data for these 19 CSC sources is shown in Table 4.

Three of the CSC sources matched to Hyads have >300 net counts in the broad band. For these sources we performed spectral analysis to extract unabsorbed f_X as well as plasma parameters (see Section 3.5). The extracted spectroscopic information is included in Table 5.

---

[17] Stelzer et al. (2000) found X-ray flares in the detections of 12 Hyads. The L_X values Stelzer & Neuhäuser (2001) published for these 12 stars exclude X-ray counts during the flares.

[18] We do not show a figure with X-ray observations of Hyads because they are are too scattered in the sky.

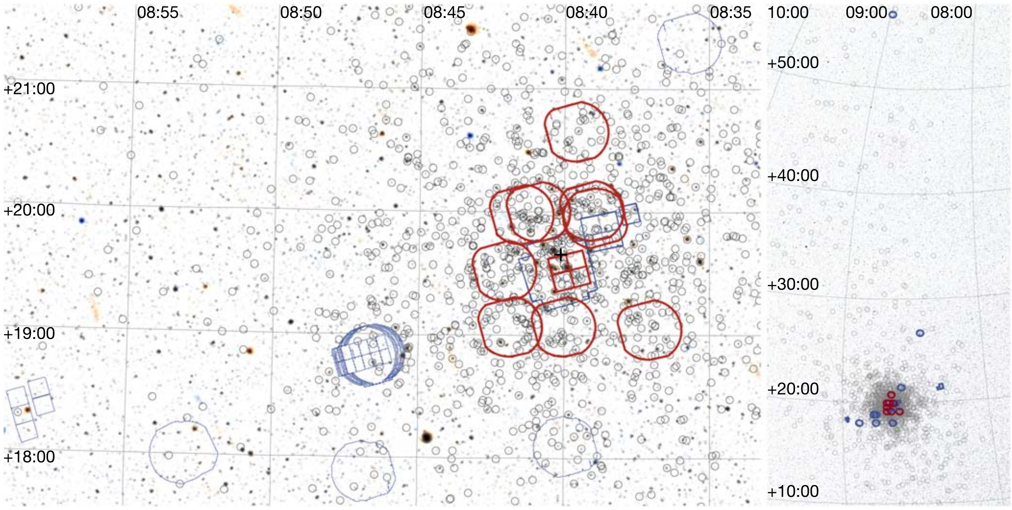

Figure 5. Left: Footprints of X-ray observations in the field of view of Praesepe: three with the Chandra ACIS camera and 24 with the XMM EPIC camera. Red footprints indicate observations for which one of the co-authors is the P.I., and blue footprints, other publicly available observations. The gray circles indicate cluster members. A black plus symbol indicates the cluster center. Each XMM footprint represents the combined contours of the usable parts of the EPIC pn and MOS cameras. Right: Zoomed out view of Praesepe, to display eight additional footprints (one Chandra and seven XMM) along a tidal tail of Praesepe, including one at $\delta > +50°$, and six that completely overlap. A Panoramic Survey Telescope And Rapid Response System (PanSTARRS) color image serves as the background on both panels.

Table 4
Log of Chandra and XMM Observations of Praesepe and Hyades

Cluster	Instrument	ObsIDs	P.I.	Start Date	Duration[a] (s)	Nominal Aimpoint α_{J2000}	Nominal Aimpoint δ_{J2000}	Roll (°)	Filter/ Data Mode
Praesepe	EPIC	0101440401	Pallavicini	2000–11	48,310	08:39:58.0	+19:32:29.0	106.2	Thick/Med[b]
Praesepe	EPIC	0721620101	Agüeros	2013–10	71,800	08:39:00.0	+19:57:00.0	103.0	Thin1
Praesepe	ACIS-I	17254–17257	Drake, J.	2015–05	191,560	08:39:50.0	+19:31:41.0	255.6–256.2	VFaint
Praesepe	EPIC	0863710201	Núñez	2021–04	32,000	08:39:32.0	+20:39:20.3	283.6	Medium
Hyades	HRC-1	2554	Ayres	2001–12	17,900	04:35:55.2	+16:30:33.0	288.3	⋯
Hyades	EPIC	0762760601	Agüeros	2015–09	17,000	04:33:27.0	+13:02:43.5	82.3	Thin1

Notes. This table is available in its entirety in the electronic edition of the ApJ. Six rows are shown here for guidance regarding its form and content.
[a] Exposure time before any filtering is applied.
[b] The first filter is for the MOS cameras and the second for the pn camera.

(This table is available in its entirety in machine-readable form.)

Table 5
Spectral Fits for the Highest X-Ray Count Chandra, Swift, and XMM Sources

Source ID	IAU Name	kT (keV)	Metal Abund.	N_H (10^{21}) (cm^{-2})	Flux (10^{-14}) (erg cm^{-2} s^{-1})	χ^2_ν	d.o.f.
107851101010001	4XMM J041802.0+181522	0.68 ± 0.02	0.54 ± 0.08	⋯	41.36 ± 3.05	1.99	227
107619211010001	4XMM J083656.2+185747	0.76 ± 0.03	0.09 ± 0.02	⋯	5.83 ± 0.45	1.06	121
107216201010012	4XMM J083915.7+200413	0.61 ± 0.05	0.05 ± 0.02	⋯	3.58 ± 0.56	0.81	53
⋯	XMMU J083952.7+203046	0.72 ± 0.09	0.05 ± 0.03	1.08 ± 0.36	4.68 ± 1.44	0.71	49
⋯	CXOU J042138.5+201809	0.98 ± 0.07	0.27 ± 0.13	⋯	4.61 ± 1.25	1.51	24

Note. Results of all acceptable spectral fits for our highest-count X-ray sources using a one-temperature APEC model. All fits included the XSPEC model TBABS to account for ISM extinction, and we give the best fit atomic hydrogen column density N_H in the cases where freeing this parameter resulted in a better fit. We also show the derived unabsorbed flux in the 0.1–2.4 keV band. Finally, we give for each fit its reduced chi-square (χ^2_ν) and degrees of freedom (d.o.f.). This table is available in its entirety in the electronic edition of the ApJ. Five rows are shown here for guidance regarding its form and content.

(This table is available in its entirety in machine-readable form.)

3.2.2. *Chandra Source Extraction with CIAO*

The CSC 2.0 only includes observations through the end of 2014. For Chandra pointings obtained after this cutoff date, we performed our own data reduction and source extraction using the Chandra Interactive Analysis of Observations (CIAO, Fruscione et al. 2006, we used CIAO v.4.13 and CALDB v.4.9.5) tools. Table 4 provides the basic information about all the Chandra pointings described next.

New Chandra *Observations*—The central field of Praesepe was observed four separate times with the same pointing and similar roll angle between 2015 May and 2015 Jun with the Advanced CCD Imaging Spectrometer (ACIS; Garmire 2003) for a total of 191.6 ks (Proposal 16200863, PI: J. Drake). The four ACIS-I chips were used in Very Faint telemetry mode to improve the screening of background events and thus increase the sensitivity of ACIS to faint sources (Vikhlinin 2001). The exposure-weighted average aimpoint of the $16'.9 \times 16'.9$ ACIS-I field of view is $\alpha = 08^{h}39^{m}50^{s}.2$, $\delta = +19^{\circ}31'05''.00$ (J2000). Figure 5 shows the combined footprint of this observation, plus an archival Chandra observation and new and archival XMM observations (see Section 3.3).

Two M dwarf Hyads, LP 415-19 (2MASS J04214435+2024105) and 2MASS J04214586+2023446, half an arcminute apart, were observed 12 separate times with the same pointing and varying roll angles between 2020 November and 2020 December, for a total of 218.7 ks (Proposal 22200351, PI: Agüeros). We used the ACIS-S3 chip, plus optional S2, I0, and I1 chips, in Very Faint telemetry mode. The exposure-weighted average aimpoint of the combined field of view is $\alpha = 04^{h}21^{m}45^{s}.2$, $\delta = +20^{\circ}23'55''.8$ (J2000). In addition to these two M dwarfs, we detected another M dwarf, 2MASS J04213829+2018102, that serendipitously fell within the field of view of the combined pointings.

The M dwarf Hyad 2MASS J04351354+2008014 was observed six separate times with the same pointing and differing roll angles during between 2021 January and 2021 October, for a total of 175.1 ks (Proposal 22200351, PI: Agüeros). We used the ACIS-S3 chip, plus optional S2, I0, and I1 chips, in Very Faint telemetry mode. The exposure-weighted average aimpoint of the combined field of view is $\alpha = 04^{h}35^{m}13^{s}.6$, $\delta = +20^{\circ}07'59''.9$ (J2000).

Lastly, three K dwarf Hyads, StKM 1-393 (2MASS J03390791+2822560), BD+05 526 (2MASS J03400754+0552286), and HD 286363 (2MASS J03550142+1229081), and one G0 dwarf Hyad, HD 265537 (2MASS J06531311+2119128), were observed individually in 2020 and 2021 as part of the Chandra Cool Targets program[19] (Proposal 20201075, PI: Agüeros). In each observation, we used the ACIS-S3 chip in Very Faint telemetry mode. Each star was observed for 10.0 ks.

Using CIAO on the New Chandra *Observations*—We performed the following steps on each one of the recent Chandra observations. We started by running `chandra_repro`. We did not use very faint correction, as we wanted to avoid excluding potentially good events in modestly bright point sources. Next, we corrected the absolute astrometry of the observations. To do this, we ran `wavdetect` with a false-probability threshold of 10^{-6} on the observations to produce a conservative list of point sources. We then used a list of high quality (PH_QUAL = AAA) 2MASS sources and the tool `reproject_aspect` to register the astrometry of the observations to the astrometric frame of 2MASS. We used a $3''$ matching radius and residual rejection limit of $0''.6$.

In the cases where observations were broken down into several pointings, we ran the steps above on the longest pointing, and then we ran `wavdetect` and `reproject_aspect` on the rest of the pointings to register their astrometry to that of the longest pointing. Next, we merged the individual pointings using `merge_obs` and produced merged events in the soft, hard, and broad bands.

We created point-spread function (PSF) maps for the observations. In the cases with more than one pointing, we combined the individual PSF maps using `dmimgfilt` and selecting the minimum PSF map size out of the individual pointings at each pixel. This last step allows us to detect point sources that may be smaller than the mean size, but still larger than the local PSF in the individual pointing maps.

Subsequently, we ran `wavdetect` for the three energy bands using the PSF map and using a less stringent false-probability threshold of 10^{-5}, to allow for a nonnegligible number of spurious sources to be included in the initial source candidate list. We consolidated the resulting three lists of sources by matching them against each other using a $2''$ matching radius for sources with off-axis angle $\theta < 5'$ and $4''$ for sources with $\theta > 5'$. For matched sources, we adopted the source region description, in order of priority, from the broad, soft, or hard band list. We then visually inspected the consolidated source list to discard sources that overlapped significantly with others or sources characterized by ellipse regions that deviated significantly from the local PSF (e.g., minor axis $\approx 0''$). Next, we used a $15''$ matching radius to find optical counterparts in our cluster catalogs for the X-ray sources. The largest offset radius was $6''.5$ (for a source at an off-axis angle of $\approx 9'$); all other offset radii were below $3''.5$.

We ran `srcflux` to extract X-ray source count rates for the three energy bands. We then used our own ECFs (see Section 4.3) and our adopted individual distances to calculate f_X and L_X in the 0.1–2.4 keV band. Three of our sources extracted with CIAO have >300 net counts in the broad band. As for the bright CSC sources described above, we performed spectral analysis on these sources to extract unabsorbed f_X values as well as plasma parameters (see Section 3.5). The extracted spectroscopic information is included in Table 5.

Lastly, we ran `glvary` on each source, which searches for X-ray variability using the Gregory–Loredo algorithm. We inspected the light curves of the six sources we have with a probability of variability $\geqslant 0.9$ (considered to be definitely variable). We found X-ray flares in five of the six light curves. In such cases, we filtered them out (see Section 3.6) and then re-ran `srcflux` to re-extract the X-ray photometry and properties of the sources.

In total, we matched X-ray sources from these recent Chandra observations to 19 Praesepe stars and eight Hyads in our catalogs. Table 3 includes the X-ray information for these 27 X-ray sources.

3.3. XMM-Newton Observations

3.3.1. Data from the XMM Serendipitous Source Catalog

We searched for X-ray counterparts to our cluster stars in the latest version of the XMM Serendipitous Source Catalog (4XMM-DR11, Webb et al. 2020) from observations with the EPIC instrument. We cross-matched the list of individual detections (which use the DETID naming convention) in the 4XMM catalog and our cluster catalogs using a $15''$ radius. We found 4XMM counterparts to 315 Praesepe stars and 110 Hyads. Like with CSC (see Section 3.2.1), we estimated the number of likely false matches by shifting the X-ray source positions in steps of $25''$ out to $5'$ in all directions and re-matched them to the cluster catalogs using the same $15''$ radius

---

[19] https://cxc.harvard.edu/proposer/CCTs.html

used before. We found the median number of false matches to be 21 (≈5% of our matched 4XMM sources) with a median offset of 10″. In our final 4XMM-cluster catalogs matches, we flag those with radii >10″—there are eight Praesepe matches (all for the same star) in this category—as likely false matches. All 110 Hyad matches, on the other hand, have matching radii <6″.

From 4XMM, we obtained count rates in the basic energy bands 1 through 5, which together span the energy range 0.2–12.0 keV, and then combined bands 1 through 3 to create a soft band, 4 and 5 to create a hard band, and 1 through 5 to create the broad band. Additionally, we obtained some other information about the X-ray sources, such as detection likelihoods and variability flags (see Table 3). We used the published count rates, our own ECF (see Section 4.3), and our adopted individual distances to calculate f_X and L_X in the 0.1–2.4 keV band. Information about the original XMM observations that collected the data for these 425 4XMM sources is shown in Table 4.

Of the 4XMM X-ray sources matched to cluster stars, 129 had >300 net counts in the broad band for the pn camera or >500 net counts in the broad band for the combined pn and MOS cameras. For these sources we performed spectral analysis to extract unabsorbed f_X as well as plasma parameters (see Section 3.5). The extracted spectroscopic information is included in Table 5.

We inspected the light curves for all 4XMM sources with flags indicating variability. We found 28 sources with X-ray flares in their light curves. In such cases, we filtered the flare events out (see Section 3.6) and then re-extracted the X-ray photometry and properties of the sources. Table 3 includes the X-ray information for all the 4XMM sources.

3.3.2. XMM Source Extraction with SAS

The 4XMM-DR11 catalog only includes observations through the end of 2020. For the XMM pointing we obtained after this cutoff date, we performed our own data reduction and source extraction using the XMM Science Analysis System (SAS v19.0, Gabriel et al. 2004) tools. Table 4 provides the basic information about this XMM recent pointing.

Furthermore, due to the automated nature of the 4XMM-DR11 catalog pipeline, some faint point-like sources may have been discarded as spurious detections. As some of our cluster stars are expected to be very X-ray faint, we performed our own data reduction of ten archival XMM observations, all targeting the cluster core, to verify that no X-ray faint source be left behind.

New XMM Observation—The slow-rotating Praesepe K3 dwarf JS 297 (2MASS J08393203+2039203) was observed in 2021 Apr for 32.0 ks (Proposal 86371, PI: Núñez). We used the EPIC cameras with the medium filter. The aimpoint of the field of view is $\alpha = 08^h39^m32\overset{s}{.}0$, $\delta = +20°39'20\overset{''}{.}3$ (J2000) and the roll angle is $283\overset{\circ}{.}6$. In addition to this K dwarf, we detected ten other Praesepe dwarfs (one F, one G, one K, and seven M types) that serendipitously fell within the field of view of this observation, as we describe next.

Using SAS on New and Archival XMM Observations—We used SAS to reduce the recent observation—plus ten archival observations targeting the core of Praesepe—with the most up-to-date calibration. We started by applying standard filters to event files. Next, we created filtered event files for the three EPIC cameras by excluding times when the global count rate in the MOS1 camera increased beyond ≈2.5 counts sec^{-1}. Finally, we used the `edetect_chain` task to perform source detection on both MOS and pn images simultaneously. The algorithm in `edetect_chain` runs a sliding box source detection (`eboxdetect`), then computes maximum likelihood analysis to prune the initial source list (`emldetect`).

The 4XMM SAS pipeline uses the five basic energy bands 0.2–0.5, 0.5–0.1, 1.0–2.0, 2.0–4.5, and 4.5–12.0 keV (bands 1 through 5) for source detection and extraction. We used instead the broader energy bands 0.2–2.0 and 2.0–12.0, plus the total band 0.2–12.0 keV. We adopted these three bands, which correspond to 4XMM bands 6, 7, and 8, as the soft, hard, and broad bands, respectively. An image with a broader energy band will include a higher number of source counts than one with a narrower band; for a very faint source, this increase in source counts may be significant. Therefore, the source detection routines may be able to pick up fainter sources in broader bands. At the same time, a broadband image will also include a higher number of background counts. As a compromise, we increased the detection likelihood threshold in the detection algorithm from 6—the value used in the automatic SAS pipeline—to 8. Furthermore, although `edetect_chain` performs simultaneous source detection across all bands and detectors, we did not require sources to be detected in all three cameras. As, for example, there are several dead chips on the MOS1 camera, this would severely limit our available area for detection.

We cross-matched the resulting X-ray source list with our cluster catalogs using a 15″ tolerance radius. From the new XMM observation (not included in the 4XMM catalog), we matched eleven X-ray sources to Praesepe counterparts. One of these matched sources had enough source counts to perform spectral analysis (see Section 3.5). Table 3 includes information for these eleven sources.

From our SAS reductions of the archival observations of the core of Praesepe, we found 34 X-ray counterparts to Praesepe stars that are not present in the 4XMM catalog. The maximum likelihood values for these 34 sources are in the range 8.2–140.0; the source with the highest likelihood was detected only with the pn camera. Table 3 includes information for these 34 sources. One of the 34 sources has a likelihood of being an extended source of 9.1, and we therefore flag this source as a likely extended source in this Table.

3.4. Data from the Swift XRT Point Source Catalog

We searched for X-ray counterparts to our cluster stars in the latest version of the Swift XRT Point Source Catalog (2SXPS, Evans et al. 2020b). This catalog includes observations through 2018 Aug, which covers eleven observations from our proposal to observe low-mass Hyads (Proposal 1215128, PI: Agüeros). We cross-matched 2SXPS and our cluster catalogs using a 15″ radius. We found 2SXPS counterparts to six Praesepe stars and 59 Hyads. Like with ROSAT (see Section 3.1.1), we estimated the number of likely false matches by shifting the X-ray source positions by 25″ out to 3′ in all directions and re-matched them to the cluster catalogs using the same 15″ radius used before. We found that the median number of false matches is one (≈2% of our matched 2SXPS sources) with a median offset of 10″. None of our 2SXPS matches merited a “likely mismatch” flag (Column 28 of Table 3).

From the 2SXPS catalog we obtained count rates in the 0.3–1.0, 1.0–2.0, and 2.0-10.0 keV bands. We then combined the first two bands to create the soft band, adopted the third band as the hard band, and combined all three bands to create the broad band. Additionally, we obtained some other information about the X-ray sources, such as hardness ratios, detection likelihoods, and variability flags (see Table 3). We used the published count rates, our own ECF (see Section 4.3), and our adopted individual distances to calculate f_X and L_X in the 0.1–2.4 keV band.

Three of the 2SXPS sources had >300 source counts in the broad band. For these sources, we performed spectral analysis to extract unabsorbed f_X as well as plasma parameters (see Section 3.5). The extracted spectroscopic information is included in Table 5.

3.5. X-Ray Spectral Fitting and Properties

We performed spectral analysis on six Chandra, three Swift, and 130 XMM sources, for a total of 139. To be included in spectral fitting, we required an X-ray source to have at least 300 counts[20] in either Chandra ACIS, Swift XRT, or XMM EPIC pn cameras; we also included XMM sources with at least 500 combined counts in the three EPIC cameras.

Of the 139 X-ray spectra, 75 are of Praesepe stars and 64 are of Hyads, including 89 total spectra for candidate/confirmed binaries. Also, seven of the 139 are cluster giants, and one is a candidate white dwarf–M6 dwarf binary (2MASS J03040207+0045512, Becker et al. 2011). We excluded these eight non-main-sequence stars from our analysis.

We used the CIAO tool Sherpa (v. 4.13.0, Freeman et al. 2001; Burke et al. 2021) to perform the spectral analysis. We fitted the spectra with an XSPEC one-temperature (1T) APEC optically thin plasma emission spectrum model. We combined the APEC model with ISM absorption model TBabs to account for extinction by neutral atomic hydrogen (N_H). We binned the spectra by 20 counts per bin for sources with more than 1000 counts, and by 15, for those with fewer than 1000 counts. We then fitted the spectra using the χ^2 statistic with the Gehrels variance function and Sherpa's *levmar* optimization method. We obtained 1σ confidence intervals of all free parameters by computing the co-variance matrices.

Most XMM sources had up to three spectra from the same observation, one EPIC pn and two MOS spectra. In such cases, we performed the spectral fit for each source using all available spectra simultaneously.

For each source, we ran the fit twice. First, we ran it by setting the N_H parameter to that of the star's cluster: 1.50×10^{20} cm^{-2} for Praesepe and 5.50×10^{18} cm^{-2} for Hyades, derived using our adopted $E(B-V)$ values for the two clusters (see Section 2.4) and $N_H[\text{cm}^{-2}/A_v] = 1.79 \times 10^{21}$ (Predehl & Schmitt 1995). Then, we freed the N_H parameter and ran the fit again. We considered the fit with the reduced χ^2 statistic (χ^2_ν) closest to unity as the best fit. Only eleven of the 139 X-ray sources had a better spectral fit with a free N_H parameter. The resulting N_H in these eleven spectra are between 0.2 and fifteen times the value for the cluster, except one case, for which N_H is two orders of magnitude larger than that of the Hyades cluster. This X-ray source with unexpectedly large N_H is matched to the white dwarf–M6 binary mentioned above.

From each spectral fit, we also obtained values for the plasma temperature kT, metal abundance with respect to the Sun, and the unabsorbed energy flux in the 0.1–2.4 keV band. Column 26 of Table 3 identifies the X-ray sources for which we used spectral fitting to calculate their f_X. Table 5 shows the fit results for each of the 139 X-ray sources, including the χ^2_ν statistic and the degrees of freedom. Figures of our spectral fits are publicly available from the Columbia University Academic Commons, an online research repository.[21]

Figure 6 shows the metal abundance (top row) and plasma temperature (bottom row) parameters resulting from our spectral fits, drawn against $(G-K)$ color (left column), R_o number (middle column, see Section 4.2), and L_X/L_{bol} (right column, see Section 4.3) for main-sequence stars in the two clusters. There is a clear trend for metal abundances to remain less than ≈0.2 with respect to Solar for most K and M dwarfs ($G-K > 1.8$). F and G dwarfs ($G-K \lesssim 1.8$), on the other hand, show a large spread in abundance, from ≈0.1 up to ≈0.9, with an average value of ≈0.4. This trend is true for both single (gray circles) and binary stars (orange × symbols). Plasma temperature, on the other hand, appears to be constrained between 0.4 keV (4.6 MK) and ≈1.0 keV (11.6 MK) for all low-mass stars, with an average value of ≈0.7 keV (8.1 MK).

3.6. Removing X-Ray Flares

Some of the X-ray observations used in our work have exposure times long enough ($\gtrsim$30 ks) to increase the probability of catching a transient stellar flare. During an X-ray flare, the X-ray emission of a star increases significantly from the quiescent level, in some extreme cases up to 7000 times, for a couple to a few hours (e.g., Osten et al. 2010). Therefore, including the emission from the flare in the calculation of the energy flux of a source would inflate the flux value from the expected quiescent level—the latter being the more representative measurement of the magnetic activity level of a low-mass star. To obtain the most representative energy flux values for stars in our two clusters, we removed X-ray flares whenever possible from our X-ray source calculations.

First, we examined the X-ray light curves of sources with variability flags indicating a high probability of a variable source, as these are the ones most likely to include an X-ray flare. Next, we identified the flare time interval of each X-ray flare, which we defined as the time with a rapid increase in the count rate to at least 3σ from the quiescent level and lasting for at least ≈2 ks (half an hour). We then generated new event files by removing counts that occurred during the flaring time intervals. Finally, we re-extracted X-ray source parameters and photometry from the new event files.

All in all, we removed flares from five Chandra and 27 XMM sources. The average change in source count rate from pre- to post-flare removing was a decrease of ≈12%. Seven of these 32 sources had an unexpected higher count rate after we removed flares. We found that in all seven cases—all from the 4XMM catalog—we removed, in addition to an X-ray flare, noisy light curve edges caused possibly by a faulty X-ray background extraction in the 4XMM automated reduction pipeline, which resulted in episodes of negative count rates in the original light curve.

---

[20] We performed spectral fitting on sources between 100 and 300 counts, but obtained poor statistical results. We therefore excluded sources with <300 counts from our spectral analysis.

[21] Available at 10.7916/dtws-0x90.

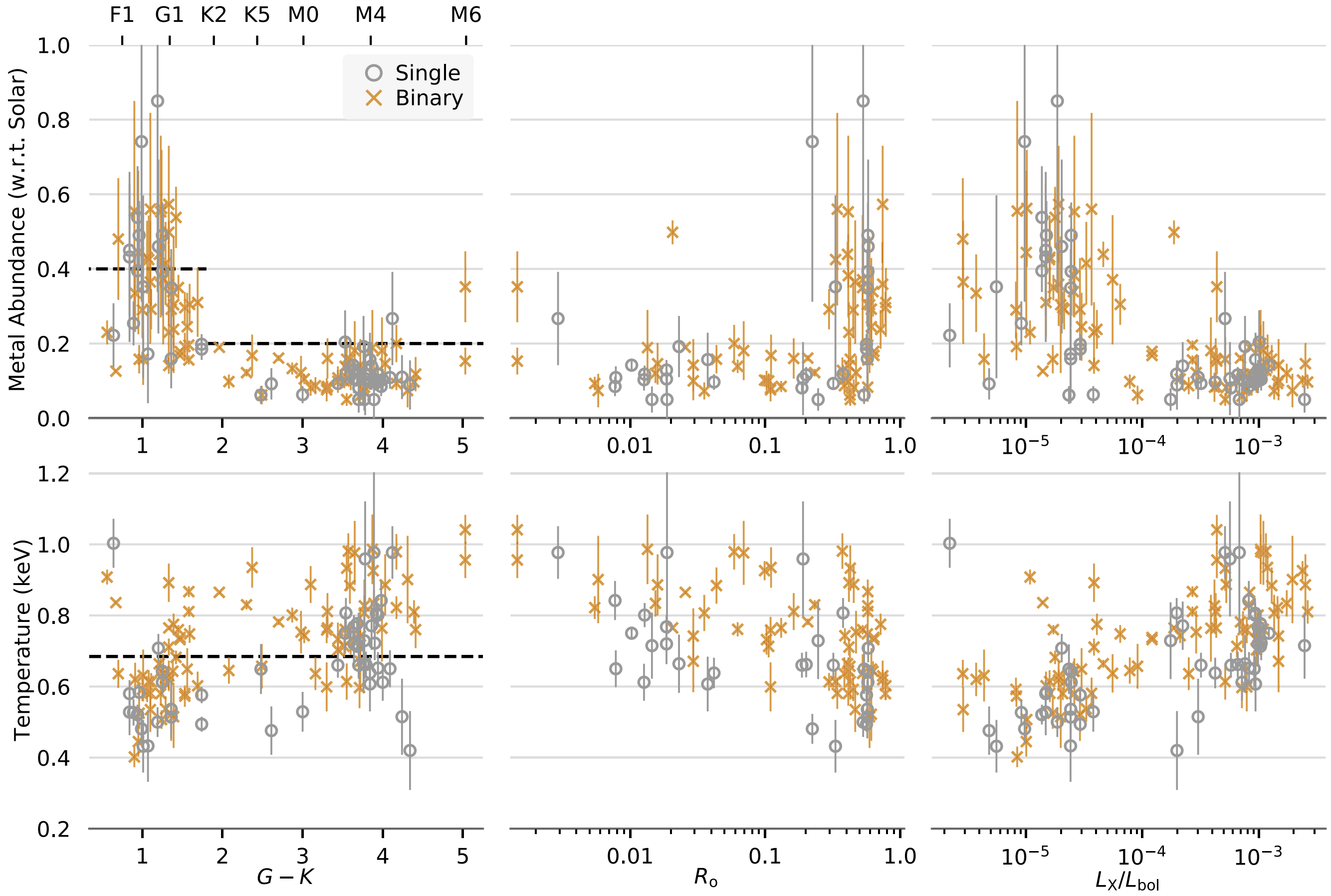

Figure 6. X-ray spectral fitting parameters for X-ray sources with >300 counts, using a one-temperature APEC model and setting the neutral hydrogen column density to the typical value for each cluster (see Section 3.5). The panels show the coronal metal abundance with respect to Solar (top row) and coronal temperature (bottom row) as a function of $(G-K)$ color (left column), R_o (middle column), and L_X/L_{bol} (right column). Gray circles indicate single members, and orange × symbols, candidate/confirmed binaries. The dash horizontal lines in the left column indicate the parameter values we assumed for the APEC model we used to derive our own ECFs to apply to low-count X-ray sources (see Section 4.3). Most K and M dwarfs have metal abundance less than ≈0.2, whereas F and G dwarfs have a large spread in abundance, from ≈0.1 up to ≈0.9. Plasma temperature is constrained between 0.4 and 1.0 keV for all dwarfs.

Column 27 of Table 3 indicates whether we removed an X-ray flare from each source to calculate its X-ray parameters and photometry. Figures of the X-ray light curves with identified flares are publicly available from the Columbia University Academic Commons.(see footnote 13)

4. Deriving Stellar Properties

4.1. Stellar Masses and Bolometric Luminosities

We calculated stellar masses m and bolometric luminosities (L_{bol}) for main-sequence members of both clusters using the empirical m–and $\log(L_{bol})$–M_G relations of E. Mamajek.[22] We linearly interpolated between the M_G values in the empirical relation to obtain m and $\log(L_{bol})$ values. The calculated m values are in the range 0.09–2.28 $M_\odot$ for Praesepe and 0.08–2.47 $M_\odot$ for Hyades. Column 31 in Table 2 includes m, and columns 33 and 34, L_{bol} and its 1σ uncertainty.

For nine of the ultracool dwarfs that we found in the literature (seven in Praesepe and two in the Hyades), we adopted m published by those authors (see Section 2.3), instead of relying on the m–M_G relation above. These nine values are in the range 0.05–0.11 $M_\odot$.

Lastly, although we calculated m and L_{bol} for candidate/confirmed binaries, we recognize that these two quantities are likely over-estimated for these stars, as there is more than one light source contributing to the brightness of the spatially unresolved stellar source.

4.2. Rossby Numbers

Studies of the rotation-activity relation typically express rotation in a mass-independent manner by substituting the Rossby number R_o for P_{rot}, as was first demonstrated by Noyes et al. (1984). R_o is given by P_{rot}/τ, where τ is the convective overturn time. We used the empirical mass–$\log(\tau)$ relation of Wright et al. (2018), which is based on P_{rot} and X-ray luminosity measurements for almost 850 stars in the mass range 0.08–1.36 $M_\odot$. Column 32 in Table 2 includes our τ estimates. With those τ values, we calculated R_o for cluster stars with a measured P_{rot}.

4.3. X-ray Luminosities

Most of the X-ray sources matched to Praesepe and Hyades stars do not have enough source counts to derive f_X from spectral fitting (see Section 3.5). For these low-count X-ray sources, we calculated ECFs using the tool WebPIMMS[23] to convert the

---

[22] Version 2021.03.02. Available at http://www.pas.rochester.edu/~emamajek/EEM_dwarf_UBVIJHK_colors_Teff.txt. Much of this table comes from Pecaut & Mamajek (2013).

[23] https://heasarc.gsfc.nasa.gov/cgi-bin/Tools/w3pimms/w3pimms.pl

instrumental count rates into unabsorbed f_X in the 0.1–2.4 keV energy band. We calculated the ECFs using a one-temperature thermal APEC model (Smith et al. 2001) with a plasma temperature[24] of 0.6845 keV and setting the following inputs specific for each X-ray source:

1. the X-ray instrument used, namely, Chandra's ACIS-I, ACIS-S, and HRC detectors, ROSAT's PSPC and HRI cameras, Swift's XRT camera, and XMM's pn and MOS EPIC cameras;
2. the Chandra cycle in which the source was detected[25];
3. the filter used with the XMM EPIC cameras (thin, medium, or thick filters);
4. the energy bands of the instrumental count rates, which are generally instrument-specific and thus different for the different X-ray missions; plus, for the case of the ROSAT catalogs we used the energy bands reported therein;
5. the N_H value assumed for each open cluster (see Section 3.5); and
6. a plasma metal abundance 16 of 0.2 for stars with $(G-K)>1.8$ and 0.4 for stars with $(G-K)\leqslant 1.8$ (see Section 3.5).

Table 6 lists all the ECFs we used for the different X-ray point sources in our X-ray catalog. Columns 24 and 25 in Table 3 include our f_X values for each X-ray source and their 1σ uncertainties, and Column 26 identifies the X-ray sources for which we derived f_X using our ECFs. We do not calculate f_X for X-ray sources with Quality Flag = "m" or "x" (Column 28 in Table 3).

There are 106 Hyads and 79 Praesepe stars with more than one f_X (and up to four). For these stars, we calculated the f_X range as a fraction of the mean: $(f_{X,\max} - f_{X,\min}) / f_{X,\text{mean}}$. The median value is 0.45, with 16th and 84th percentiles of 0.15 and 1.12. Eleven stars have values beyond 1.6 (and up to 2.8). In all eleven cases, the time span of the detections is between 15 and 25 years. We suspect, therefore, that we may be capturing Solar-type activity cycles in these stars. However, a study of such activity cycles is beyond the scope of this project.

For stars with more than one f_X, we used the error-weighted mean f_X as the adopted f_X for the star. Lastly, we converted f_X into L_X using our adopted distances. For each cluster star detected in X-rays, columns 29 and 30 in Table 2 include the adopted f_X value and its 1σ uncertainty.

Freund et al. (2020) calculated L_X values for Hyads From Chandra, ROSAT, and XMM detections. If a star had more than one X-ray detection, these authors assigned it a "best" X-ray detection to derive its L_X, instead of combining them like we did. This results in our sample having L_X uncertainties smaller than theirs for several stars. Also, they did not account for potential flares in their X-ray detections like we did, which results in several of these flaring Hyads having lower L_X in our catalog. Furthermore, in their ECFs, these authors assumed an APEC temperature of 0.2725 keV and a metal abundance of 1.0 for all stars, compared to our temperature of 0.6845 keV and abundance of 0.2 or 0.4.

To compare our L_X values against those in Freund et al. (2020) for the same stars, we had to account for the difference in energy ranges used to calculate L_X (their 0.2–12.0 keV versus our 0.1–2.4 keV). Using PIMMS, we found that one must increase f_X by 16.3% to go from 0.2–12.0 keV to 0.1–2.4 keV, everything else being equal. After applying this correction, we found a median offset in luminosity of ≈11% between our L_X values and theirs, with our values being larger on average. Figure 7 compares our L_X to those in Freund et al. (2020), highlighting stars for which we removed flares L_X (filled red circles). The systematic offset between our L_X and those of Freund et al. (2020) can be explained by the difference in assumed APEC parameter values: increasing the plasma temperature from 0.2725 keV to 0.6845 keV increases the resulting f_X values by up to 20%, and decreasing the plasma abundance from 1.0 to 0.2 decreases the resulting f_X values by up to 5%.

5. Results and Discussion

5.1. X-Ray Spectral Parameters

Beginning with the Advanced Satellite for Cosmology and Astrophysics (ASCA) and Extreme Ultraviolet Explorer (EUVE) missions, studies of both low- and high-resolution EUV and X-ray spectra of low-mass stars have revealed that the chemical composition of the corona differs from that of the underlying photosphere (e.g., Drake et al. 1996; Brinkman et al. 2001; Güdel 2007; Testa 2010). Long documented in the case of the Sun, this chemical abundance anomaly is referred to as the "First Ionization Potential (FIP) Effect": elements with low FIP (FIP ⩽10 eV-, e.g., Si, Mg, Fe) are enhanced by factors of 2–4 relative to elements with high FIP (FIP ⩾10 eV; e.g., N, Ne, Ar). In the stellar case, stars with fairly low, solar-like magnetic activity levels exhibit a solar-like FIP effect (e.g., Drake et al. 1997). Instead, more active stars exhibit the reverse, and the low FIP metals are generally depleted relative to high-FIP elements (e.g., Brinkman et al. 2001; Drake & Kashyap 2001).

More recent studies with high-resolution X-ray spectra have also uncovered a spectral type dependence of the FIP effect, and it is not yet clear whether the depletion or enhancement of metals is mostly controlled by magnetic activity level (e.g., Telleschi et al. 2005; García-Alvarez et al. 2009), or by the change in outer convection zone properties with spectral type (e.g., Wood & Linsky 2010; Wood et al. 2012; Wood & Laming 2013).

The FIP and inverse FIP effects are not yet fully understood, but are likely related to one or more mechanisms of coronal heating (e.g., Drake et al. 2002; Testa et al. 2015). The most promising model to date cites the ponderomotive force on ions in the chromosphere associated with magnetohydrodynamic waves (Laming 2015).

Our results show a clear correlation between spectral type and coronal metal abundance. In our sample of Praesepe and Hyades stars, K and M dwarfs ($G-K \gtrsim 1.8$) display very low abundances, whereas F and G dwarfs ($G-K \lesssim 1.8$) display higher abundances (see upper left panel of Figure 6). We find similar correlations with R_o and L_X/L_{bol}: fast rotators ($R_o \lesssim 0.2$) have very low abundances, and vice versa (upper middle panel), and the more active stars ($L_X/L_{\text{bol}} \gtrsim 10^{-4}$) have very low abundances, and vice versa (upper left panel).

---

[24] The PIMMS models only have solutions for discrete values of the input parameters. The closest of these discrete values to our average plasma temperature is 0.6845 keV, and to our average metal abundances are 0.2 and 0.4 Solar.

[25] We used https://cxc.harvard.edu/toolkit/pimms.jsp for Chandra's ECFs, because it accounts for the evolution of the effective areas of the Chandra detectors.

Table 6
ECFs Used For the Low-Count X-Ray Sources

Observatory	Instrument	Energy Band[a]	Other Describers[b]	Praesepe		Hyades	
				Abundance 0.2	Abundance 0.4	Abundance 0.2	Abundance 0.4
Chandra	ACIS-I	0.5–7.0	Cycle 4	⋯	⋯	7.314E−12	6.462E−12
			Cycle 8	9.956E−12	8.842E−12	9.672E−12	8.584E−12
			Cycle 9	9.972E−12	8.856E−12	⋯	⋯
			Cycle 15	⋯	⋯	1.278E−11	1.140E−11
			Cycle 16	1.529E−11	1.370E−11	⋯	⋯
	ACIS-S	0.5–7.0	Cycle 3	⋯	⋯	4.240E−12	3.798E−12
			Cycle 8	⋯	⋯	5.354E−12	4.740E−12
			Cycle 9	5.554E−12	4.918E−12	⋯	⋯
			Cycle 13	⋯	⋯	6.048E−12	5.342E−12
			Cycle 14	6.084E−12	5.554E−12	6.082E−12	5.372E−12
			Cycle 20	⋯	⋯	2.020E−11	1.843E−11
			Cycle 21	⋯	⋯	1.808E−11	1.647E−11
			Cycle 22	⋯	⋯	2.120E−11	1.947E−11
	HRC	0.1–10.0	Cycle 3	⋯	⋯	8.218E−12	8.126E−12
			Cycle 4	⋯	⋯	8.140E−12	7.980E−12
ROSAT	PSPC	0.1–2.0	2RXS/2RXP	1.141E−11	1.101E−11	6.950E−12	7.314E−12
		0.4–2.0	R95	1.630E−11	1.431E−11	⋯	⋯
		0.1–1.8	S95	⋯	⋯	6.928E−12	7.294E−12
		0.1–2.0	S01	⋯	⋯	6.904E−12	7.266E−12
	HRI	0.2–2.4	1RXH	3.578E−11	3.258E−11	3.074E−11	2.880E−11
Swift	XRT	0.3–10.0	PC	3.202E−11	2.976E−11	2.998E−11	2.804E−11
XMM	pn	0.2–12.0	Thin	1.559E−12	1.511E−12	1.322E−12	1.315E−12
			Medium	1.632E−12	1.560E−12	1.425E−12	1.390E−12
			Thick	2.248E−12	2.094E−12	2.055E−12	1.935E−12
	MOS	0.2–12.0	Thin	7.186E−12	6.800E−12	6.452E−12	6.204E−12
			Medium	7.454E−12	6.996E−12	6.800E−12	6.462E−12
			Thick	9.322E−12	8.634E−12	8.686E−12	8.102E−12

Notes. All ECFs have units erg cm^{-2} cts^{-1} and produce unabsorbed f_X values in the 0.1–2.4 keV band. We calculated two sets of ECFs using a 1T APEC model: one set adopted a metal abundance of 0.2 (columns 5 and 7), and another set adopted a metal abundance of 0.4 (columns 6 and 8). See Section 4.3 for more details.All ECFs have units erg cm^{-2} cts^{-1} and produce unabsorbed f_X values in the 0.1–2.4 keV band. We calculated two sets of ECFs using a 1T APEC model: one set adopted a metal abundance of 0.2 (columns 5 and 7), and another set adopted a metal abundance of 0.4 (columns 6 and 8). See Section 4.3 for more details.

[a] The original energy band of the instrumental count rate values.

[b] Cycle number for Chandra; catalog for ROSAT: R95 is Randich & Schmitt (1995), S95 is Stern et al. (1995), and S01 is Stelzer & Neuhäuser (2001); operation mode for Swift; and filter type for XMM.

As will be shown in Section 5.3, spectral type, R_o, and L_X/L_{bol} are tightly correlated in our sample of ≈700 Myr old stars, as most fast rotating stars with high activity levels are K and M types, whereas most slowly spinning stars with moderate to low activity are F and G types. Therefore, we cannot completely disentangle activity level, rotation, and spectral type from their relation to coronal abundance in our sample. Nonetheless, we note that abundance has a tighter correlation with spectral type than with activity level, as evidenced by a clear shift from $\lesssim 0.2$ to an average ≈0.4 abundance in both $(G-K)$ color space and R_o space, the latter being a function of the stellar mass dependent τ parameter. Furthermore, a significant fraction of K dwarfs have similar slow rotation and low activity levels as G dwarfs, and yet in Figure 6 it is clear that all K dwarfs have abundance levels comparable to those of the fast rotating, highly active M dwarfs instead.

Studies have also found mean coronal temperature to decrease with decreasing magnetic activity levels (see review by Telleschi et al. 2005). In our sample, we observe a correlation between temperature and L_X/L_{bol} (see lower right panel of Figure 6). Temperature increases by a factor of ≈2.5 as L_X/L_{bol} increases by ≈3 orders of magnitude. In a similar study, Singh et al. (1999) found on a sample of ten low-mass field stars that temperature increased by a factor of ≈4 while L_X/L_{bol} increased by three orders of magnitude. Thus, in our sample, coronal temperature appears to be slightly less sensitive to activity levels.

A similar correlation can be observed between temperature and R_o (bottom middle panel), where stars with higher R_o, i.e., slower rotation rates and, consequently, lower activity levels, display lower coronal temperatures, more so for single stars than for binaries. The bottom left panel of Figure 6, on the other hand, shows a very weak correlation between coronal temperature and $(G-K)$ color. Rising temperature with increasing color (i.e., later spectral types) can be discerned for binaries. For single stars, the mean temperature of later types is higher, but this is accompanied by a larger spread in values.

For the most part, however, single and binary stars display very similar behaviors in Figure 6. This result appears to contradict that of Pye et al. (1994), who showed binary K dwarf Hyads being at least twice as X-ray bright as their single brethren. We note that there is a significant gap in our coverage

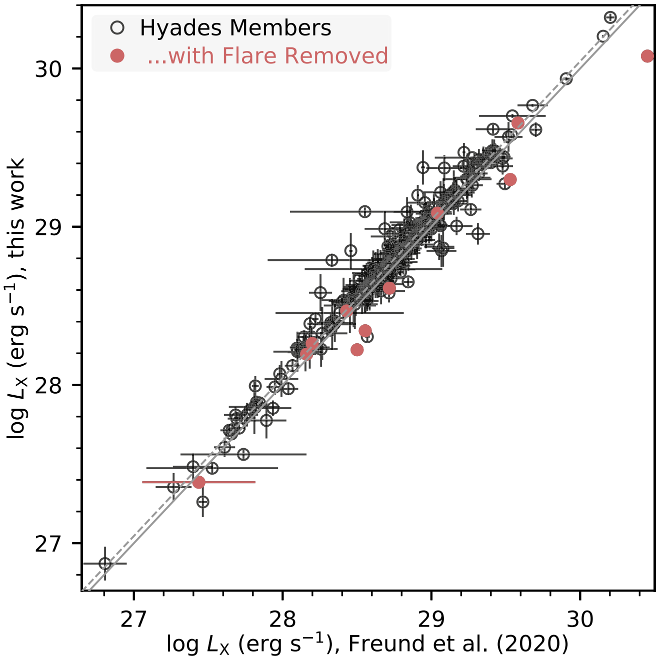

Figure 7. Comparison of L_X values derived for Hyads in Freund et al. (2020) (abscissa) vs. our L_X values for the same stars (ordinate). We account for the difference in energy range (their 0.2–12.0 keV vs. our 0.1–2.4 keV) by increasing their L_X values by 16.3%. Hyads for which we removed X-ray flares before computing their L_X are highlighted with red circles. The gray solid line is the 1:1 relation, and the gray dashed line is offset from the 1:1 relation by 11%, which corresponds to the median offset in luminosity between our L_X values and those in Freund et al. (2020).

of K and early M dwarfs ($1.8 \lesssim G - K \lesssim 3.5$) with X-ray spectral fitting parameters: in this spectral range we have only four single stars, but we have 17 binaries. And indeed, in that range binaries appear to have higher coronal temperatures than the single cohort, but with only four single stars to compare against, we cannot affirm that with a high level of confidence.

5.1.1. The Color–Rotation Plane for Single Stars

In Figure 8, we plot single Praesepe and Hyades members in $(G - K)$–$P_{\rm rot}$ space, with color indicating $L_X/L_{\rm bol}$. Stars that remain undetected in X-rays are indicated with gray triangles. We note in both clusters (although more so in Praesepe due to its broader $P_{\rm rot}$ coverage) that mid F to early G dwarfs can have similar $P_{\rm rot}$ values to some early-to-mid M dwarfs (≈M3 to M5), and yet the latter have much higher levels of magnetic activity. Furthermore, early-to-mid M dwarfs have $L_X/L_{\rm bol}$ spanning up to ≈1 order of magnitude, and yet their $P_{\rm rot}$ values span over 2 orders of magnitude (≈5 hr up to ≈25 days). Evidently, some saturation mechanism is preventing the fastest rotators from increasing their X-ray emission beyond a certain $L_X/L_{\rm bol}$ level, as we will see more clearly in Section 5.3.

Lastly, stars with RUWE > 1.4 do not stand out in the $(G - K)$–$P_{\rm rot}$ plane (highlighted with black edges in Figure 8). If these high-RUWE stars are indeed unresolved intermediate binaries, Figure 8 tells us that their spin down evolution has not been greatly affected, if at all, by the companion.

5.2. The Distribution of X-Ray Emission

Figure 9 shows the relation between X-ray emission, in the form of $L_X/L_{\rm bol}$ (upper panels) and L_X (lower panels), and $(G - K)$ color for Praesepe (left panels) and Hyades (right panels) stars. We calculate in Table 7 the $L_X/L_{\rm bol}$ and L_X median, 16th, and 84th percentiles of several spectral type ranges for both single and binary stars. $L_X/L_{\rm bol}$ follows a narrow increasing $L_X/L_{\rm bol}$-color relation from F through early G types, then spreads—if not remaining flat—between early G and early M types, and then narrows again beyond early M types. This is true for both Praesepe and Hyades stars, as well as single (gray circles) and candidate/confirmed binary (orange× symbols) stars. For the latter, there is a larger spread in $L_X/L_{\rm bol}$ compared to singletons at the relatively flat $L_X/L_{\rm bol}$ region between early G and early M types.

In L_X space (bottom panels), we find a global trend for later spectral types to have lower L_X, which is not surprising as the latter depends on the stellar luminosity and the size of the stellar corona and, thus, on m and radius. We note that mid M dwarfs can have equivalent L_X levels as some F and early G dwarfs, even though F types can have stellar radii ≈5 times larger than mid M types, and hence, up to 25 times larger surface areas. The small sizes of the highly active M dwarfs in our sample is compensated by their brighter X-ray emission reflected by their smaller $R_{\rm o}$ and largely saturated activity (see Section 5.3). As we found that coronal temperatures varied only weakly across spectral types (see bottom left panel of Figure 6), this brighter emission cannot simply be due to hotter coronae in the M dwarfs. The brighter X-ray emission from M dwarfs is therefore likely driven by higher number of active regions and/or a significant difference in magnetic topology (e.g., Lang et al. 2012).

5.2.1. X-Ray Emission of Singles versus Binaries

In Section 5.1, we noted that there were only small differences in the X-ray emission characteristics, namely, coronal abundance and temperature, between single and binary stars. To better visualize any systematic difference between singles versus binaries in $L_X/L_{\rm bol}$ and L_X, we performed 1000 Monte Carlo iterations of Δ median log $L_X/L_{\rm bol}$ = (median log $L_X/L_{\rm bol})_{\rm binaries}$ − (median log $L_X/L_{\rm bol})_{\rm singles}$ for each spectral type range in Table 7. At each iteration, we added noise to all $L_X/L_{\rm bol}$ measurements, drawn from a Gaussian with width equal to the uncertainty of each measurement, and re-measured the median value. We repeated the same process in log L_X space. We show in Figure 10 the mean and standard deviation of Δ from our Monte Carlo results for each cluster and spectral type range.

If we consider the case of unresolved binary systems including two X-ray emitters, their unresolved L_X would be higher compared to those for single stars. In the scenario of their total X-ray emission coming from two stars each with activity levels commensurate to those of single stars, their total L_X would be twice that of an equivalent single star. On the other hand, in the scenario of the binary components having experienced past and/or present interactions, resulting in inflated levels of activity, their total L_X would be even greater than that of the previous scenario. In both scenarios, our measured $L_{\rm bol}$ would also be inflated for unresolved binaries, as our $L_{\rm bol}$ are derived from M_G (see Section 4.1). In the extreme case of equal mass binary systems, their total $L_{\rm bol}$ would be inflated anywhere between 20% and 60% (assuming that equal mass binaries lie 0.375 in M_G above the single main sequence, see, e.g., Rampalli et al. 2021) compared to their hypothetical individual $L_{\rm bol}$ values. All in all, for the scenario of binaries without inflated activity, the combined effect would be $L_X/L_{\rm bol}$

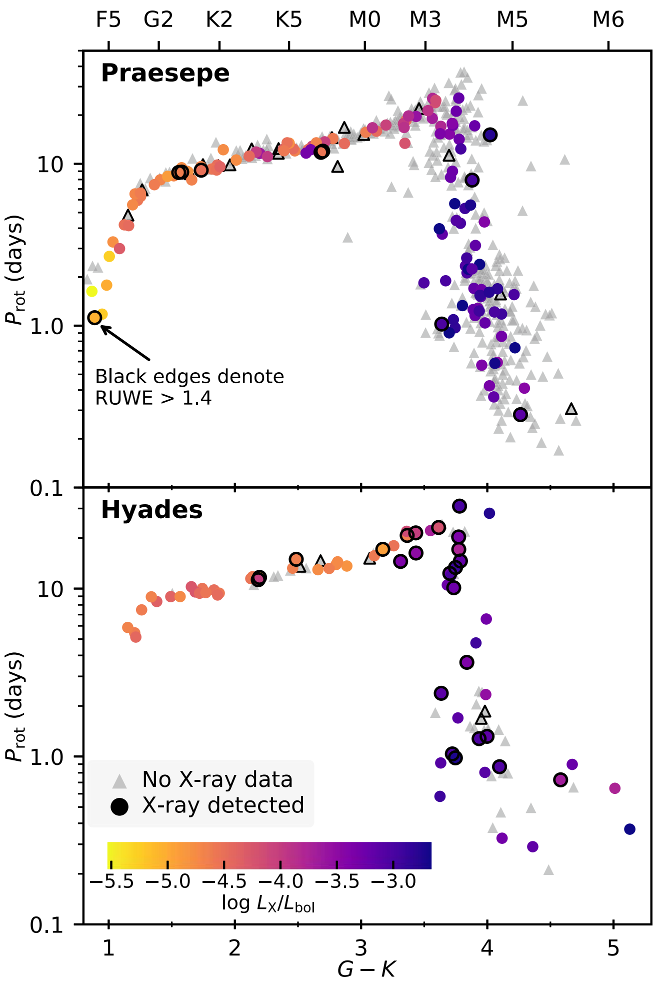

Figure 8. $P_{\rm rot}$ vs. $(G-K)$ color for single Praesepe (top panel) and Hyades (bottom panel) stars. Circles indicate stars with an $L_X/L_{\rm bol}$ measurement. Gray triangles indicate stars without X-ray data. The circles are color-coded according to their log $L_X/L_{\rm bol}$ following the colorbar at the bottom left. Symbols with black edges are single stars with RUWE > 1.4.

anywhere between 1.2 and 1.7× higher for binaries than for singles, or up to ≈0.2 orders of magnitude.

The top panel shows that binaries and singles have similar $L_X/L_{\rm bol}$ values—the largest differences are smaller than 0.5 orders of magnitude, and most differences are within 0.2 orders of magnitude, both above and below zero. We believe these minor differences can be explained mostly by the small sample sizes and by the inherent noise around measuring the X-ray emission of a main-sequence dwarf, by virtue of both short-term (e.g., flaring) and long-term (e.g., Solar-type activity cycles) variability. Such inherent noise in our result obscures the expected intrinsic over-luminosity of binaries in the hypothetical scenario described above.

The result in L_X space is almost identical, with two marginal exceptions. First, K5–K9 binaries in the Hyades are ≈0.7 orders of magnitude more luminous than their single counterparts. Pye et al. (1994) had found that the X-ray luminosity function of K binaries in the Hyades was almost one order of magnitude more luminous than that of their single counterparts. Our result, therefore, partly supports their conclusion. Second, M0–M3 binaries in Praesepe are ≈0.8 orders of magnitude more luminous than their single counterparts.

In both of these exceptions, the significant over-luminosity of the binary sample cannot be explained only by assuming that we are capturing two or more individual—and unresolved—X-ray emitters in our binary L_X measurements. Instead, such over-luminosity suggests that binaries have higher magnetic activity levels than single stars at those spectral type ranges. Their rotational information partly corroborates this: In our sample of K5–K9 Hyads, four out of the nine known binaries with known $P_{\rm rot}$ are fast rotators ($\leqslant$5 days), whereas all seven singles with known $P_{\rm rot}$ are slow rotators ($\geqslant$10 days). It is still puzzling that the highlighted exceptions are for only one specific spectral type range and for stars in only one of the two clusters. In any event, we caution the reader about the small sizes of our spectral type subsamples in Table 7, which may lead to uncertain statistical results.

A potential additional piece of evidence of inflated magnetic activity could be found in the fraction of X-ray variable/flaring stars in our full sample of X-ray detections. The most magnetically active stars are expected to have more common flaring episodes (e.g., Kowalski et al. 2009), and thus have a higher probability of getting caught flaring or displaying large variability during an X-ray observation. Of the 963 X-ray sources we have with a variability flag, 9% are flagged as definitely variable: 36 are single members and 47 are binaries. As such, we find no strong preference for binaries to have signs of variability or flaring in X-rays over single members.

Similar to Figure 9, Figure 11 shows $L_X/L_{\rm bol}$ (upper panels) and L_X (lower panels) as a function of $(G-K)$ color for stars in our sample, this time only including stars identified as single cluster members. Colored circles are stars with $P_{\rm rot}$ measurements, identified by the color map in the upper left panel, and triangles are stars without $P_{\rm rot}$. Both clusters reveal a trend of increasing $P_{\rm rot}$ with increasing $(G-K)$ color for stars in the relatively flat $L_X/L_{\rm bol}$ region between early G and early M spectral types. For spectral types later than ≈M3, roughly coinciding with the transition between partially and fully convective stellar interiors (Chabrier & Baraffe 1997), almost all stars display fast rotation ($P_{\rm rot} \ll 10$ days) and high $L_X/L_{\rm bol}$. Furthermore, both F and mid-to-late M dwarfs can have equivalent $P_{\rm rot}$ values, and yet stars in the latter cohort display $L_X/L_{\rm bol}$ values that are two orders of magnitude higher than the F dwarfs in the same cluster.

Interestingly, and analogous to what we find in the color–$P_{\rm rot}$ plane (Figure 8), there is no significant offset in $L_X/L_{\rm bol}$ or L_X between single stars with RUWE $\leqslant$ 1.4 and > 1.4. The latter—highlighted with black edges in Figure 11—could be unresolved intermediate binaries (see Section 2.6), which means that their X-ray detections could be a combination of X-ray emission from two (or more) separate sources. In the extreme case of two equally X-ray bright emitters, their $L_X/L_{\rm bol}$ and L_X values would appear over-luminous compared to their single counterparts by 0.3 in log space, everything else remaining equal. Such a relatively small difference is largely obscured by the intrinsic noise in our sample data. However, the fact that there is no widespread large X-ray over-luminosity in stars with RUWE > 1.4 suggests that levels of magnetic activity in these potential binaries are not inflated compared to those in single stars.

5.2.2. X-Ray Outlier in the Hyades

The F8 Hyad HD 50554 (2MASS J06544283+2414441) appears under-luminous in X-rays by at least two orders of

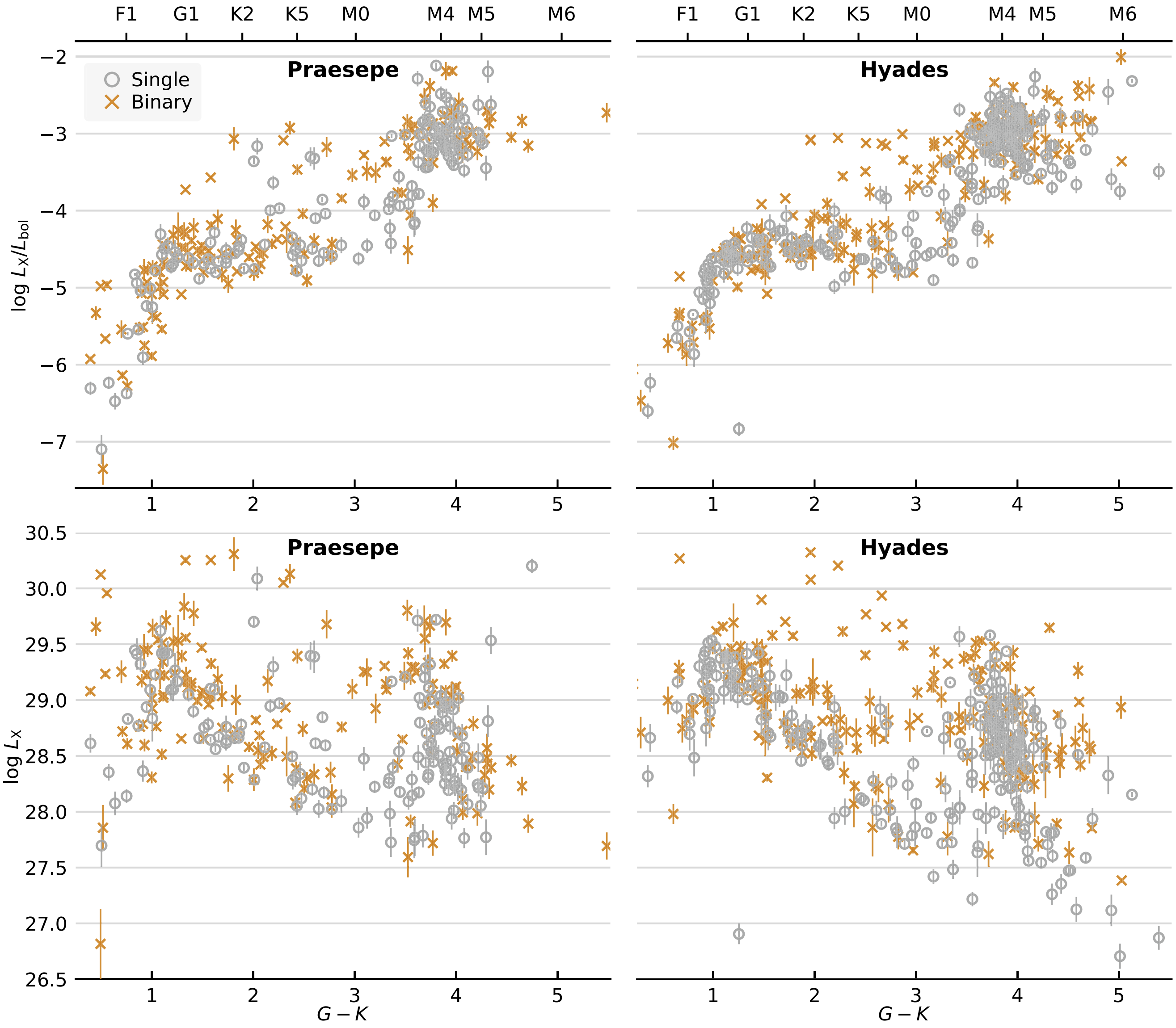

Figure 9. L_X/L_{bol} (top panels) and L_X (bottom) vs. $(G-K)$ color for Praesepe (left panels) and Hyades (right) stars. Gray circles indicate single members, and orange× symbols, candidate/confirmed binaries. Stars, both single and binary, follow a narrow increasing L_X/L_{bol} sequence from F through early G that then spreads between G and early M types, and narrows again beyond early M types.

magnitude compared to its peers (log $L_X/L_{bol} = -6.83$, log $[L_X/\mathrm{erg\ s}^{-1}] = 26.9$; see right panels of Figure 9). Sanz-Forcada et al. (2010) estimated an age of 12.2 Gyr for this star, and Kains et al. (2011), 4.7 Gyr, based on a surrounding debris disk detected in the far-infrared. Our faint L_X value for this star appears to corroborate an age much older than that of the Hyades. We included this star in our Hyades catalog because it is considered a trailing tail star in the Röser et al. (2019) GDR2 Hyades catalog. However, these authors noted that almost 14% of trailing tail stars in their catalog are statistically expected to be contaminants. Given the estimated ages in the literature and its significant under-luminosity in X-rays, we consider this star a likely contaminant in our Hyades membership catalog, and therefore exclude it from our calculations in Table 7.

5.3. The Relationship Between X-Ray Emission and Rotation

A more direct way to analyze the link between coronal activity and rotation in low-mass stars is by characterizing the relationship between L_X/L_{bol} and R_o (see Section 4.2). We break down our sample of cluster stars into single and binary stars, both for each cluster and combined, to characterize the R_o–L_X/L_{bol} relation.

To obtain a very clean sample of single stars, we exclude those with RUWE > 1.4, the latter considered to be likely unresolved intermediate binaries (see Section 2.6). Instead, we include these high-RUWE stars in our sample of cluster binaries. As we noted in Section 5.2.1, the X-ray emission from high-RUWE stars may be dominated, partially or entirely, by only one of the members of the potential binary system. As we cannot resolve the system in X-rays or optically, we therefore consider these stars as potential contaminants in our analysis of the rotation-activity relation in single stars.

We also exclude cluster stars with $m \gtrsim 1.3\ M_\odot$ (≈F5 type and earlier) to probe the R_o–L_X/L_{bol} relation. Although main-sequence stars with m up to ≈1.6 $M_\odot$(≈F0 type) can have an outer convective zone (Böhm-Vitense & Dettmann 1980), their magnetic activity ceases to be correlated with rotation. It is, thus, not dominated by a solar-like dynamo, but by fossil magnetic fields instead (e.g., Böhm-Vitense et al. 2002;

Table 7
L_X/L_{bol} and L_X Statistics

Sample	Sp. Type	$N_\star$	log L_X/L_{bol}	log L_X
		Praesepe		
Singles	F0–F4	8	$-5.39^{+0.44}_{-0.48}$	$28.88^{+0.52}_{-0.47}$
	F5–F9	12	$-4.60^{+0.12}_{-0.23}$	$29.20^{+0.22}_{-0.11}$
	G0–G4	…	…	…
	G5–G9	8	$-4.67^{+0.23}_{-0.12}$	$28.71^{+0.34}_{-0.07}$
	K0–K4	19	$-4.51^{+0.58}_{-0.18}$	$28.66^{+0.35}_{-0.35}$
	K5–K9	12	$-4.45^{+0.72}_{-0.15}$	$28.27^{+0.71}_{-0.19}$
	M0–M3.0	37	$-3.43^{+0.59}_{-0.65}$	$28.44^{+0.68}_{-0.47}$
	M3.5–M5	50	$-3.00^{+0.33}_{-0.24}$	$28.48^{+0.46}_{-0.27}$
Binaries	F0–F4	11	$-5.51^{+0.64}_{-0.40}$	$29.17^{+0.16}_{-0.50}$
	F5–F9	18	$-4.80^{+0.34}_{-0.57}$	$29.22^{+0.31}_{-0.34}$
	G0–G4	12	$-4.48^{+0.22}_{-0.22}$	$29.19^{+0.60}_{-0.11}$
	G5–G9	12	$-4.55^{+0.38}_{-0.14}$	$29.05^{+0.31}_{-0.14}$
	K0–K4	22	$-4.45^{+0.26}_{-0.31}$	$28.68^{+0.43}_{-0.28}$
	K5–K9	11	$-4.39^{+0.88}_{-0.20}$	$28.35^{+0.86}_{-0.17}$
	M0–M3.0	26	$-3.23^{+0.39}_{-0.54}$	$29.21^{+0.21}_{-0.56}$
	M3.5–M5	33	$-2.97^{+0.25}_{-0.18}$	$28.57^{+0.51}_{-0.33}$
		Hyades		
Singles	F0–F4	17	$-5.06^{+0.24}_{-0.43}$	$29.15^{+0.21}_{-0.38}$
	F5–F9	20	$-4.61^{+0.11}_{-0.17}$	$29.27^{+0.12}_{-0.17}$
	G0–G4	7	$-4.41^{+0.07}_{-0.19}$	$29.16^{+0.26}_{-0.03}$
	G5–G9	11	$-4.37^{+0.14}_{-0.28}$	$29.02^{+0.13}_{-0.26}$
	K0–K4	20	$-4.45^{+0.12}_{-0.12}$	$28.61^{+0.15}_{-0.16}$
	K5–K9	17	$-4.62^{+0.44}_{-0.12}$	$28.07^{+0.27}_{-0.23}$
	M0–M3.0	50	$-3.30^{+0.37}_{-0.92}$	$28.60^{+0.43}_{-0.68}$
	M3.5–M5	95	$-3.02^{+0.29}_{-0.35}$	$28.52^{+0.34}_{-0.71}$
Binaries	F0–F4	8	$-5.51^{+0.10}_{-0.24}$	$28.92^{+0.08}_{-0.12}$
	F5–F9	15	$-4.53^{+0.13}_{-0.26}$	$29.41^{+0.17}_{-0.08}$
	G0–G4	10	$-4.60^{+0.16}_{-0.15}$	$29.16^{+0.22}_{-0.12}$
	G5–G9	18	$-4.46^{+0.13}_{-0.25}$	$29.07^{+0.41}_{-0.31}$
	K0–K4	32	$-4.42^{+0.36}_{-0.15}$	$28.74^{+0.44}_{-0.19}$
	K5–K9	18	$-4.20^{+1.06}_{-0.41}$	$28.75^{+0.91}_{-0.75}$
	M0–M3.0	33	$-3.14^{+0.25}_{-0.52}$	$29.00^{+0.36}_{-0.37}$
	M3.5–M5	53	$-2.86^{+0.26}_{-0.40}$	$28.59^{+0.45}_{-0.56}$

Note. The quoted values are median, 16th, and 84th percentiles.

Kochukhov 2003; Walter & Linsky 1986; Wolff & Heasley 1987).

We parameterize the R_o–L_X/L_{bol} relationship as a flat region connected to a power law. For stars with $R_o \leqslant R_{o,sat}$, activity is constant—i.e., saturated—and equal to $(L_X/L_{bol})_{sat}$. Above $R_{o,sat}$, activity declines as a power law with index β, and is, therefore, unsaturated. Functionally, this corresponds to

$$\frac{L_X}{L_{bol}} = \begin{cases} \left(\frac{L_X}{L_{bol}}\right)_{sat} & \text{if } R_o \leqslant R_{o,sat} \\ C R_o^{\beta} & \text{if } R_o > R_{o,sat} \end{cases} \tag{1}$$

where C is a constant. This model has been widely used in the literature (e.g., Randich 2000; Wright et al. 2011; Douglas et al. 2014; Núñez et al. 2015).

We use the open-source Markov-chain Monte Carlo (MCMC) package `emcee` (Foreman-Mackey et al. 2013) to fit this three-parameter model to our data. Like in the `emcee` implementation by Magaudda et al. (2020), we allow for a nuisance parameter f to account for underestimated errors.[26]

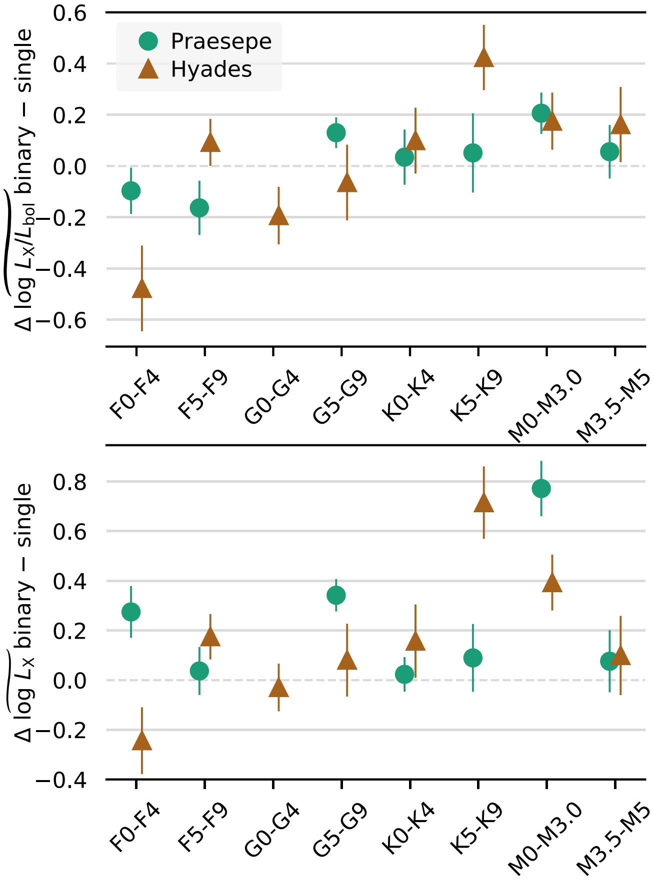

Figure 10. Top: Mean value, plus 95% confidence interval, of the median log L_X/L_{bol} for binaries minus the median log L_X/L_{bol} for single members in Praesepe (green circles) and Hyades (brown triangles) for each spectral type bin of Table 7, using a Monte Carlo simulation. Bottom: Same as above, but in log L_X space. We find only marginal differences in X-ray activity—more evident in L_X space and for a couple of spectral type bins—between the single and binary populations.

We assume flat priors over each parameter and use 300 walkers, each taking 5000 steps in their MCMC chain, to infer maximum likelihood parameters. Our results are presented in Figure 12. The posterior distributions for each parameter and 2D correlations between pairs of parameters from each fit are included in a Figure Set in Appendix A; 200 random samples from these distributions are shown in Figure 12, along with the maximum a posteriori model. In all cases, the nuisance factor f converges to ≈ 0.1, which suggests that our L_X/L_{bol} uncertainties are underestimated by no more than $\approx 10\%$.

The $(L_X/L_{bol})_{sat}$, $R_{o,sat}$, and β parameters corresponding to the maximum a posteriori model are presented in Table 8 for the six subsamples we show in Figure 12, and are also annotated in each panel in the Figure. The stated values correspond to the 50th percentiles of the results and the uncertainties are the 16th and 84th percentiles. We selected these percentiles to be consistent with 1σ Gaussian uncertainties, even though our one-dimensional 1D posterior probability distributions are not Gaussian.

5.3.1. X-Ray Emission and Rotation in Singles versus Binaries

Stars in close binary systems may have their spin down history affected by the companion, leading to circularized

---

[26] See https://emcee.readthedocs.io/en/develop/user/line/.

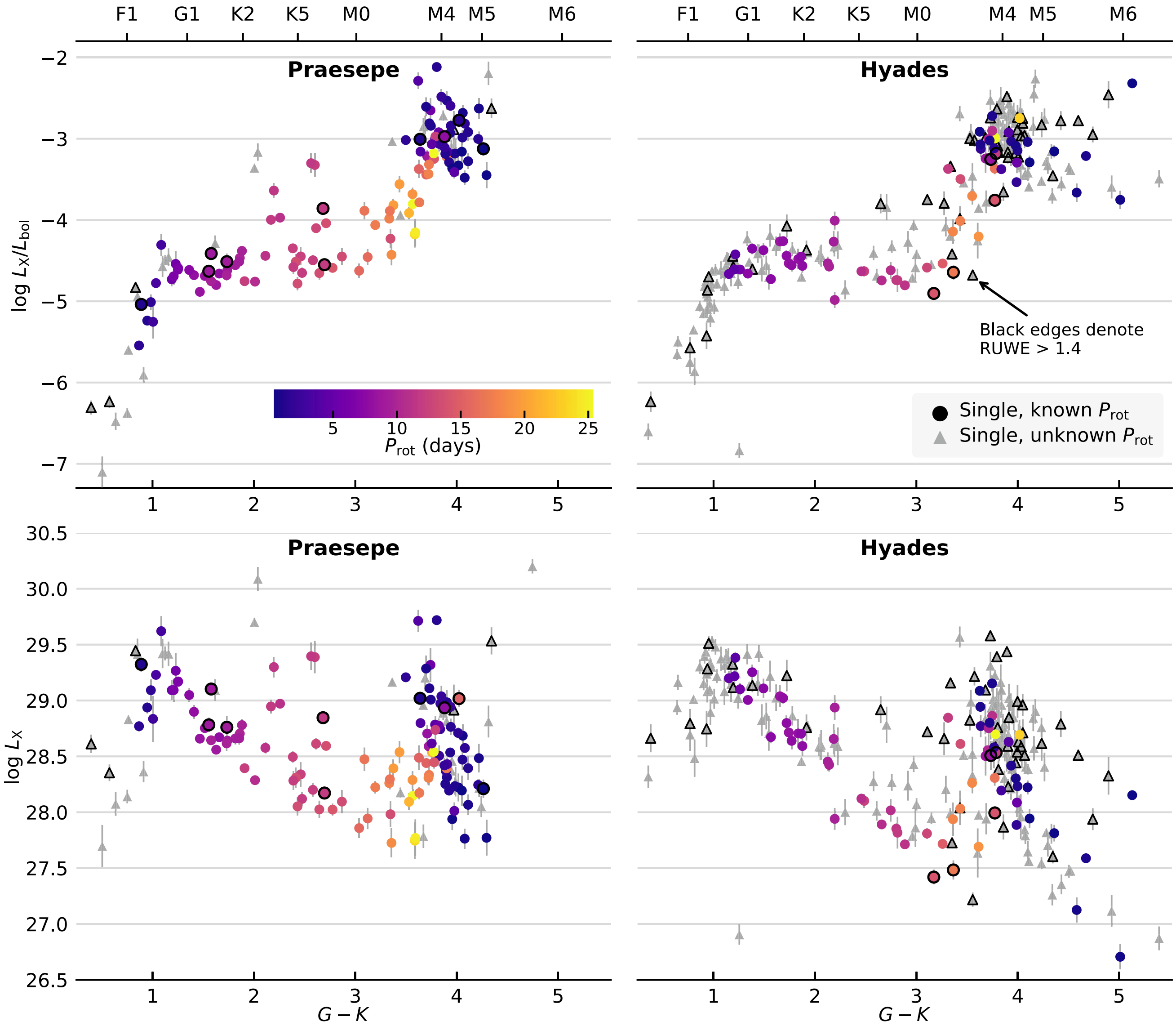

Figure 11. Same as Figure 9, but plotting only stars with no binary flags. Circles indicate stars for which we have a P_{rot}, and gray triangles, stars without P_{rot}. The circles are color-coded according to the P_{rot} value using the colorbar in the top right panel. Symbols with black edges are single stars with RUWE > 1.4. Stars appear to plateau in L_X/L_{bol} between early G and early M spectral types, even as they display increasing P_{rot} toward later types.

orbits and synchronized P_{rot}, the latter resulting in either faster or slower rotation than their single stellar counterparts at the same age (Counselman 1973; Meibom & Mathieu 2005; Zahn 2008; Fleming et al. 2019). This could lead to higher or lower X-ray activity in binaries, compared to coeval single stars. For example, and as we noted in Section 5.2.1, Pye et al. (1994) found that K dwarf binaries in the Hyades are more than twice as luminous as their single counterparts. Also, if the binaries are close enough to each other, it is also possible that their magnetic fields may directly interact.

Based on our fits in Section 5.3, the relationships between coronal activity and R_o are mostly similar for both our single and binary subsamples. $(L_X/L_{bol})_{sat} \approx 10^{-3}$ in all subsamples, with singles versus binaries agreeing within 1σ in their saturation level. The $R_{o,sat}$ thresholds fall within the approximate narrow range 0.13–0.23, also agreeing within 1σ. However, β is steeper for single stars than for binaries: β falls between −3.24 and −3.93 for single stars, and between −2.22 and −2.82 for binaries.

As we discussed in Section 5.2.1, if we assumed that both components in unresolved binaries are X-ray emitters, their combined X-ray emission and M_G would translate into higher $(L_X/L_{bol})_{sat}$ for binaries than for singles. For unresolved binaries, their R_o values are smaller than for equivalent single stars by anywhere between ≈10% and 50%, as our τ are derived from stellar masses, which in turn are derived from M_G (see Section 4.1). The combined, almost uniform upward shift in L_X/L_{bol} and rightward shift in R_o for binaries in the R_o–L_X/L_{bol} plane would translate into a negligible change in β compared to single stars. This shift would only affect $R_{o,sat}$, increasing it by up to 50%.

In Table 8 (and Figure 12) we see that the binary subsamples have higher $(L_X/L_{bol})_{sat}$ than the single counterparts by no more than 1.3×, and their values agree within 1σ with one another. The large spread in activity in the saturated regime in all subsamples may be partially hiding what would otherwise be a more statistically significant over-luminosity of binaries over singles in this regime.

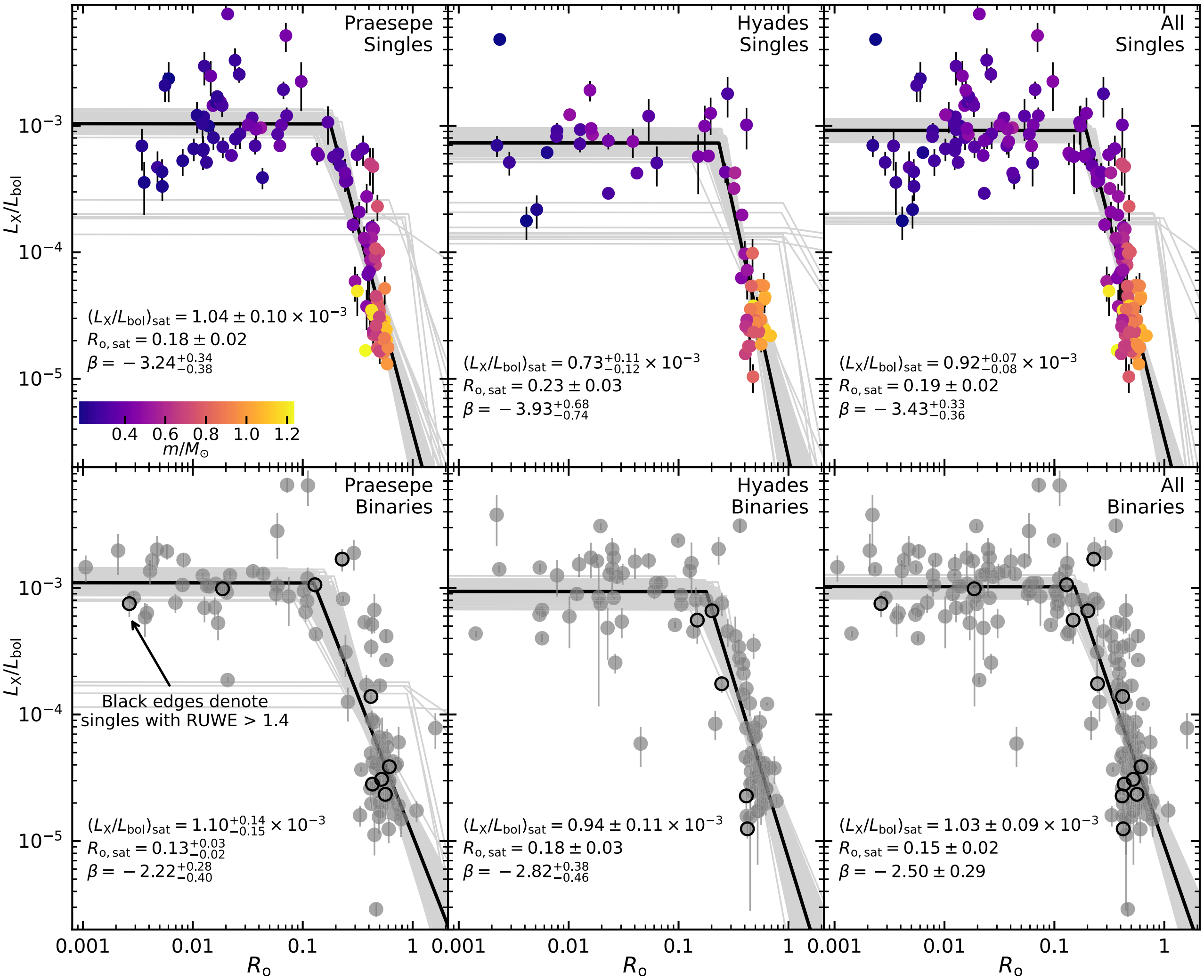

Figure 12. L_X/L_{bol} vs. R_o for stars in Praesepe (left column), Hyades (middle), and both clusters (right). The top row shows single stars, and the bottom row shows candidate/confirmed binaries. This latter set includes stars with no binary flags but with RUWE > 1.4 (indicated with solid black circles). Single stars are color-coded by their m following the colorbar in the top left panel. The solid black line in each panel is the maximum a posteriori fit from the MCMC algorithm, and the gray lines are 200 random samples from the posterior probability distributions. The fit result of the three parameters, $(L_X/L_{bol})_{sat}$, $R_{o,sat}$, and β, are annotated in each panel. We show in the Appendix the marginalized posterior probability distributions from the MCMC analysis for each fit. The power-law index β in the unsaturated regime for single stars is significantly steeper than that for binary stars, the latter being closer to the canonical $\beta \approx -2$ from other studies in the literature.

Table 8
Rossby–L_X/L_{bol} Relation Fitting Results

Sample	$N_\star$	$(L_X/L_{bol})_{sat}$ (10^{-3})	$R_{o,sat}$	β
		Singles		
Praesepe	114	1.04 ± 0.10	0.18 ± 0.02	$-3.24^{+0.34}_{-0.38}$
Hyades	63	$0.73^{+0.11}_{-0.12}$	0.23 ± 0.03	$-3.93^{+0.68}_{-0.74}$
All	177	$0.92^{+0.07}_{-0.08}$	0.19 ± 0.02	$-3.43^{+0.33}_{-0.36}$
		Binaries & with RUWE > 1.4		
Praesepe	107	$1.10^{+0.14}_{-0.15}$	$0.13^{+0.03}_{-0.02}$	$-2.22^{+0.28}_{-0.40}$
Hyades	98	0.94 ± 0.11	0.18 ± 0.03	$-2.82^{+0.38}_{-0.46}$
All	205	1.03 ± 0.09	0.15 ± 0.02	-2.50 ± 0.29

On the other hand, in the subsamples of Praesepe stars and of combined (i.e., "All") cluster stars, β values are shallower for binaries than for singles, disagreeing by at least 1σ, and $R_{o,sat}$ values are statistically equivalent for both binaries and singles. Only in the Hyades, the singles and binaries subsamples have β within 1σ: $3.93^{+0.68}_{-0.74}$ versus $-2.82^{+0.38}_{-0.46}$, respectively. Freund et al. (2020) found $\beta = -2.12 \pm 0.60$ in their Hyades study of f_X/f_{bol} versus R_o, which is statistically closer to our β for binary Hyads than for single Hyads. We note that these authors did not exclude X-ray flares from their calculations of X-ray emission and did not systematically apply binary flags to their sample of stars.

Both the persistent shallower β values in our binaries subsamples and the indistinguishable $R_{o,sat}$ values in both singles and binaries may be driven by the larger scatter—both in L_X/L_{bol} and R_o—in their unsaturated regime compared to our subsamples of single stars, which leads to a poorer power-law fit. In our unresolved binaries, there is no way to appropriately assign L_X and L_{bol} values to the individual components of the binary systems. Even if we assume a first order approach and split L_X evenly between the binary components, we are still left with the complication of assigning R_o to only one of them, as the adopted P_{rot} only captures one rotating signal. In short, the ambiguity in the X-ray emission level of stars flagged as binaries or with RUWE > 1.4 makes the sample presented in the bottom row of Figure 12 inappropriate to study the R_o–L_X/L_{bol} relation in stars with secular angular momentum evolution.

5.3.2. Saturation and Supersaturation

As we noted earlier, the level of saturation in L_X/L_{bol} lies at $\approx 10^{-3}$ for all the subsamples we examined. There is a large spread, a little over one order of magnitude, in L_X/L_{bol} in the saturated regime, particularly in our sample of Praesepe stars. This finding is similar to the large sample in Wright et al. (2011), in which a mix of cluster and field stars have a saturated L_X/L_{bol} value of $\approx 10^{-3}$ and a spread of about 1.5 orders of magnitude.

We inspected the X-ray nature of stars that are either too under- or over-luminous in the saturated regime, to determine whether systematic issues were contributing to the spread in L_X/L_{bol}. We find no correlation between L_X/L_{bol} and X-ray observatory or source counts. That is, the under/over-luminosity is not a function of X-ray instrument or exposure times, which leads us to believe that the noise in L_X/L_{bol} in the saturated regime is intrinsic to the stars, due perhaps to unaccounted X-ray flaring or to activity cycles similar to that observed in the Sun.

To test for supersaturation, a phenomenon usually observed in stars with $R_o \lesssim 0.02$, we add a secondary power law of index β_{sup} connected to the flat region in Equation (1) for $R_o < R_{o,sup}$, where $R_{o,sup}$ is the threshold R_o value between supersaturation and saturation. The results and figures of our MCMC routine on the modified five-parameter (the three parameters in Equation (1) plus β_{sup} and $R_{o,sup}$) model are included in Appendix B.

For our subsamples of single cluster stars, β_{sup} falls anywhere between 0.23 and 0.76 and $R_{o,sup} \approx 0.01$. Such values of β_{sup} could indicate that stars with $R_o < R_{o,sup}$ are supersaturated and, thus, experiencing a reduced amount of X-ray activity by virtue of their extremely fast rotation. However, we recognize that both β_{sup} and $R_{o,sup}$ are not nearly as constrained as $R_{o,sat}$ and β in the unsaturated regime—both the random samples from the posterior probability distributions and the marginalized posterior probability distributions can attest to this (see Appendix B). We therefore recognize these results as only tentative evidence for supersaturation.

Lastly, for our subsamples of binary cluster stars, β_{sup} is statistically indifferent from zero, and $R_{o,sup}$ is virtually unconstrained. If it is true that binaries show no signs of supersaturation while single stars do, then this could be interpreted as evidence for inflated levels of coronal activity in binaries with extremely fast rotation.

5.3.3. Spectral Type versus Rotation and Activity

Figure 13 shows our sample of single Praesepe and Hyades stars combined (gray circles), highlighting with colored symbols in each panel different spectral types. As can be seen in the right-most panel, *all* stars in the hypothetical supersaturated regime ($R_o \lesssim 0.01$) have spectral types later than M3.5, i.e., the fully convective stars. The smallest R_o in our sample of single stars is 0.002 ($P_{rot} \approx$7h), for the M5 and M7.5 dwarfs 2MASS J05003894+2422581 and J04351354+2008014, respectively. The latter, in particular, appears significantly brighter than its super fast rotating peers ($L_X/L_{bol} = 4.8 \times 10^{-3}$). This, in spite of the fact that we removed an X-ray flare from its detection to calculate its quiescent L_X/L_{bol} (see Section 3.6). It is possible, therefore, that we observed this ultracool dwarf during an episode of large variability and flaring activity, which would explain its over-luminosity compared to the other M dwarfs in the supersaturated regime.

We noted in Figure 8 the narrow slow-rotating sequence for single stars spanning the mid F to early M spectral types illustrating the one-to-one relationship between spectral type and rotation in Praesepe and the Hyades. Now, Figure 13 highlights the large spread in X-ray activity, as measured by L_X/L_{bol}, in these same stars. All late-F, G, and K dwarfs have practically the same R_o, and yet they cover roughly one order of magnitude in L_X/L_{bol}. Early M dwarfs (M0–M3.5) cover one order of magnitude in R_o space and two orders of magnitude in L_X/L_{bol}. Lastly, mid- and late M dwarfs (M3.5–M7), the fully convective cohort, span two orders of magnitude in R_o space (with P_{rot} values from $\approx$5 hr up to $\approx$30 days), while their spread in L_X/L_{bol} spans *only* one and a half orders of magnitude (right-most panel in Figure 13).

As our sample of Praesepe and Hyades stars is approximately coeval, we can safely assume that within the same spectral type range, the cause of the spread in L_X/L_{bol} is not a function of age. In the current paradigm of angular momentum driving the level of magnetic activity in low-mass stars, our findings illustrate the strong dependence of L_X/L_{bol} on R_o in unsaturated, partly convective dwarfs. On the other hand, in the cohort of fully convective dwarfs, a very large range in R_o translates into only a modest range in L_X/L_{bol}. It would be easy to hold their fully convective nature responsible for this behavior. However, we may just be observing an age at which only the fully convective—and a few partially convective—stars remain saturated and, thus, restricted in their activity levels by whatever mechanisms drive the saturated regime.

6. Conclusion

The Hyades and Praesepe form a crucial bridge between very young open clusters and field-age stars in the study of the evolution of rotation and activity in low-mass stars. We re-visit these two clusters to expand our understanding of the connection between rotation and coronal activity at their critical stellar age.

We start by combining several membership catalogs, including our own legacy catalogs and GDR2-based catalogs, and consolidating literature binary information on these stars. We produce a Praesepe catalog with 1739 members and a Hyades catalog with 1315 members. For these members, we collect GEDR3 *G* and 2MASS *K* and photometry and astrometry to derive stellar parameters, including stellar mass and L_{bol}. Next, we consolidate P_{rot} measurements from the literature for stars in both clusters.

To produce a comprehensive catalog of coronal activity, we search for X-ray detections of cluster members with the ROSAT, Chandra, Swift, and XMM observatories, both archival and new observations. We rely on the archival serendipitous catalogs of each observatory to obtain the X-ray flux of each detection. For ten XMM pointings, we perform our own data reduction to add 34 very faint X-ray sources that were not included in the XMM serendipitous catalog. Additionally, we reduce seven new observations from Chandra and XMM that were taken after the cutoff dates of the serendipitous catalogs.

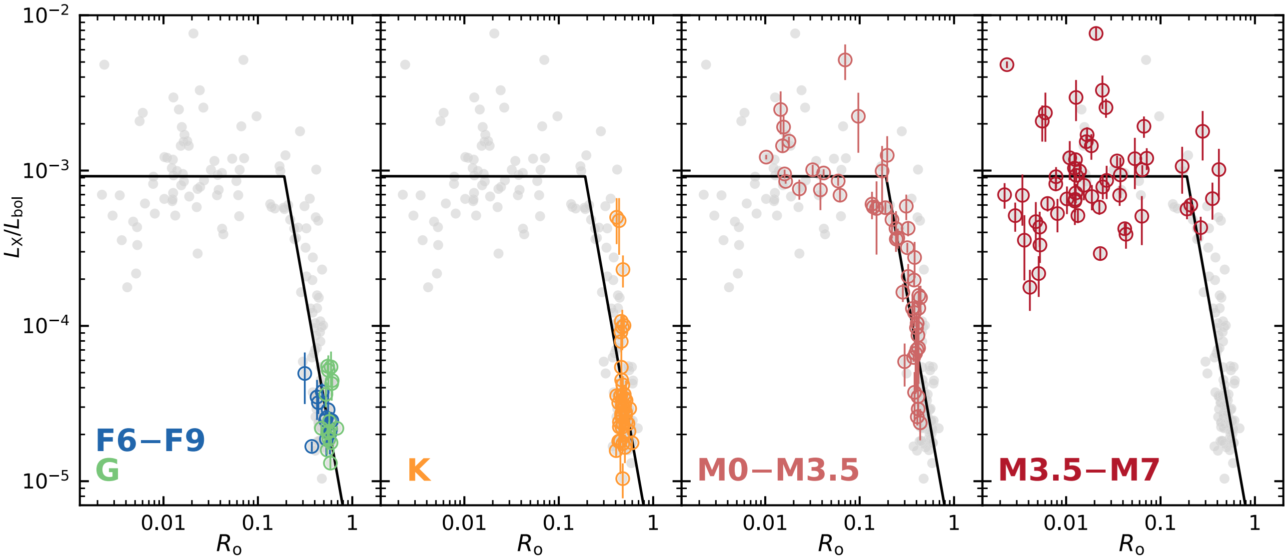

Figure 13. L_X/L_{bol} vs. R_o for single stars in Praesepe and Hyades, highlighting the different spectral types in each panel. The background gray symbols in all panels are the combined sample of single FGKM dwarfs in both Praesepe and Hyades, but excluding those with RUWE > 1.4. The solid black line in all panels is the maximum a posteriori fit from the MCMC algorithm for the full sample of single Praesepe and Hyades stars (see top right panel of Figure 12). At the age of Praesepe and Hyades, fully convective dwarfs (M3.5 and later) remain saturated in X-rays, whereas most early-to-mid M dwarfs and all late-F, G, and K dwarfs have spun down into the unsaturated regime.

We derive f_X values for each X-ray detection from the instrumental count rates using our own ECFs. For 139 X-ray sources with sufficient counts, we perform spectral analysis instead to derive f_X along with coronal temperature and metal abundance. For the 32 sources in which we identify flares in their X-ray light curves, we first remove counts from the flare events before calculating their f_X. We find no difference in the coronal parameters of binary and nonbinary cluster members. We also find a very weak correlation between spectral type and coronal temperature, and a slightly stronger positive correlation between L_X/L_{bol} and coronal temperature. More importantly, we find that coronal abundance displays a strong correlation with stellar spectral type: G and early-K dwarfs have typical abundance values of ≈0.4 Solar, while mid-K to mid-M dwarfs have values of 0.2 Solar or lower. At the age of Praesepe and Hyades, these two sets of stars coincide with the difference between slow and fast rotators, or high and low R_o numbers, thus suggesting that coronal abundance is directly linked to P_{rot} and, thus, to magnetic activity level.

We find that in both clusters L_X/L_{bol} increases from F through early G types, then flattens between early G and early M types, and then increases again beyond early M types. Binary stars show a larger spread than the single counterparts in this L_X/L_{bol} trend. In particular, late K dwarf binary Hyads are almost one order of magnitude more luminous in L_X than their single counterparts, partially supporting previous findings in the literature. Single stars with RUWE > 1.4—a threshold we adopt to indicate unresolved binaries—have the similar L_X/L_{bol} levels as stars with RUWE $\leqslant$ 1.4, suggesting that X-ray emission in the former is not significantly inflated by binary interactions compared to single stars.

In the R_o–L_X/L_{bol} plane of both clusters, we find a saturated regime, in which $L_X/L_{bol} \approx 10^{-3}$ and independent from stellar rotation for stars with $R_o \lesssim 0.1$ or 0.2, and an unsaturated regime, in which L_X/L_{bol} depends on R_o following a power law with slope β between −3.93 and −3.24 for single stars, and −2.82 and −2.22 for binaries. As L_X, L_{bol}, and R_o measurements of unresolved binary systems are ambiguous and problematic, we reiterate that the R_o–L_X/L_{bol} relation in stars with secular angular momentum evolution must be studied in samples that exclude unresolved binaries.

We find tentative evidence for supersaturation for single stars in both clusters with $0.002 < R_o \lesssim 0.01$. In this R_o regime, stars follow a power law with slope between 0.24 and 0.76. However, both the slope and the R_o threshold between supersaturation and saturation are not as well constrained as the parameters in the saturated and unsaturated regimes.

Lastly, in our large coeval sample of single known rotators with unsaturated X-ray emission, a change of 0.5 orders of magnitude in R_o translates into a change in up to two orders of magnitude in L_X/L_{bol}. This steep relationship highlights the sensitivity of coronal activity to the rotation of a star. On the other hand, fully convective stars have small R_o values spanning two orders of magnitude, and L_X/L_{bol} values, roughly one order of magnitude. The latter phenomenon may be driven by the fact that fully convective stars at the age of Praesepe and Hyades are fully within the saturated regime and, thus, restricted in their activity levels by whatever mechanisms drive saturation.

A.N. acknowledges support provided by the NSF through grant 2138089. M.A.A. acknowledges support provided by NASA through grant NNX17AD71G. J.J.D. was supported by NASA contract NAS8-39073 to the Chandra X-ray Center and thanks the Director, P. Slane, for continuing advice and support.

We estimated the spectral types used in our analysis and several figures using a $(G-K)$-spectral type relation based on the Stellar Color and Effective Temperature Sequence of E. Mamajek, available at http://www.pas.rochester.edu/~emamajek/EEM_dwarf_UBVIJHK_colors_Teff.txt (v. 2021.03.02).

This work has made use of data from the European Space Agency (ESA) mission Gaia (https://www.cosmos.esa.int/gaia), processed by the Gaia Data Processing and Analysis Consortium (DPAC, https://www.cosmos.esa.int/web/gaia/dpac/consortium). Funding for the DPAC has been provided by national institutions, in particular the institutions participating in the Gaia Multilateral Agreement.

This research has made use of the NASA/IPAC Infrared Science Archive, which is operated by the Jet Propulsion Laboratory, California Institute of Technology, under contract with the National Aeronautics and Space Administration. The Two Micron All-Sky Survey was a joint project of the University of Massachusetts and IPAC.

Funding for the Sloan Digital Sky Survey IV has been provided by the Alfred P. Sloan Foundation, the U.S. Department of Energy Office of Science, and the Participating Institutions. SDSS acknowledges support and resources from the Center for High-Performance Computing at the University of Utah. The SDSS website is www.sdss.org.

This research has made use of data obtained from the 4XMM XMM-Newton Serendipitous Source Catalog compiled by the 10 institutes of the XMM-Newton Survey Science Centre selected by ESA, and of data obtained from the Chandra Source Catalog, provided by the Chandra X-ray Center as part of the Chandra Data Archive.

This work made use of data supplied by the UK Swift Science Data Centre at the University of Leicester.

This research has made use of NASA's Astrophysics Data System Bibliographic Services, the SIMBAD database, operated at CDS, Strasbourg, France, the VizieR database of astronomical catalogs (Ochsenbein et al. 2000), and the "Aladin Sky Atlas", developed at CDS, Strasbourg Observatory, France.

Appendix A
Marginalized Posterior Probability Distributions for the MCMC Analysis of Our R_o–L_X/L_{bol} Model

We present the marginalized posterior probability distributions from the MCMC analysis we performed on six different subsamples of Praesepe and Hyades stars: single members of each cluster, binary members for each cluster, single members of both clusters combined, and binary members of both clusters combined (see Section 5.3 and Table 8). The binary samples include candidate and confirmed binaries, including single stars with RUWE > 1.4. Figure 14 shows an example of the marginalized posterior probability distributions for the subsample of single members from both clusters.

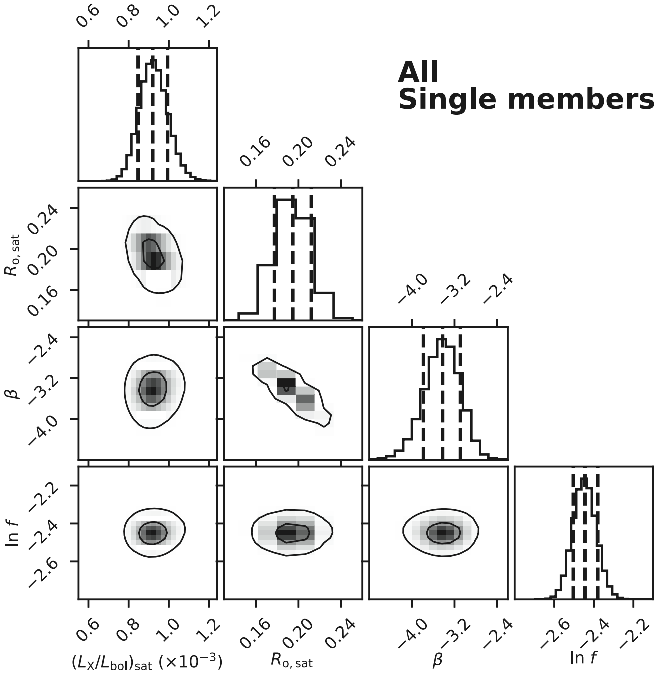

Figure 14. Marginalized posterior probability distributions from the MCMC analysis of our R_o–L_X/L_{bol} model using `emcee` for single members in both Praesepe and Hyades. The parameter values of the a posteriori model are the peaks of the one-dimensional distributions; the vertical dashed lines approximate the median and 16th, 50th, and 84th percentiles. The two-dimensional distributions illustrate covariances between parameters; the contour lines approximate the 1σ and 2σ levels of the distributions. The complete figure set, which includes an image for each of the six subsamples in Table 8, is available in the online journal.

(The complete figure set (6 images) is available.)

Appendix B MCMC Results for Our Modified R_o–L_X/L_{bol} Model with Supersaturation

We present the results and marginalized posterior probability distributions from the MCMC analysis we performed on six different subsamples of Praesepe and Hyades stars: single members of each cluster, binary members for each cluster, single members of both clusters combined, and binary members of both clusters combined, using a modified R_o–L_X/L_{bol} model that includes a secondary power law at small R_o to represent the supersaturated regime (see Section 5.3.2). Figure 15 shows the modified R_0–L_x/L_{bol} model on the six subsamples, using the same format as in Figure 12. Figure 16 shows an example of the marginalized posterior probability distributions for the subsample of single members from both clusters.

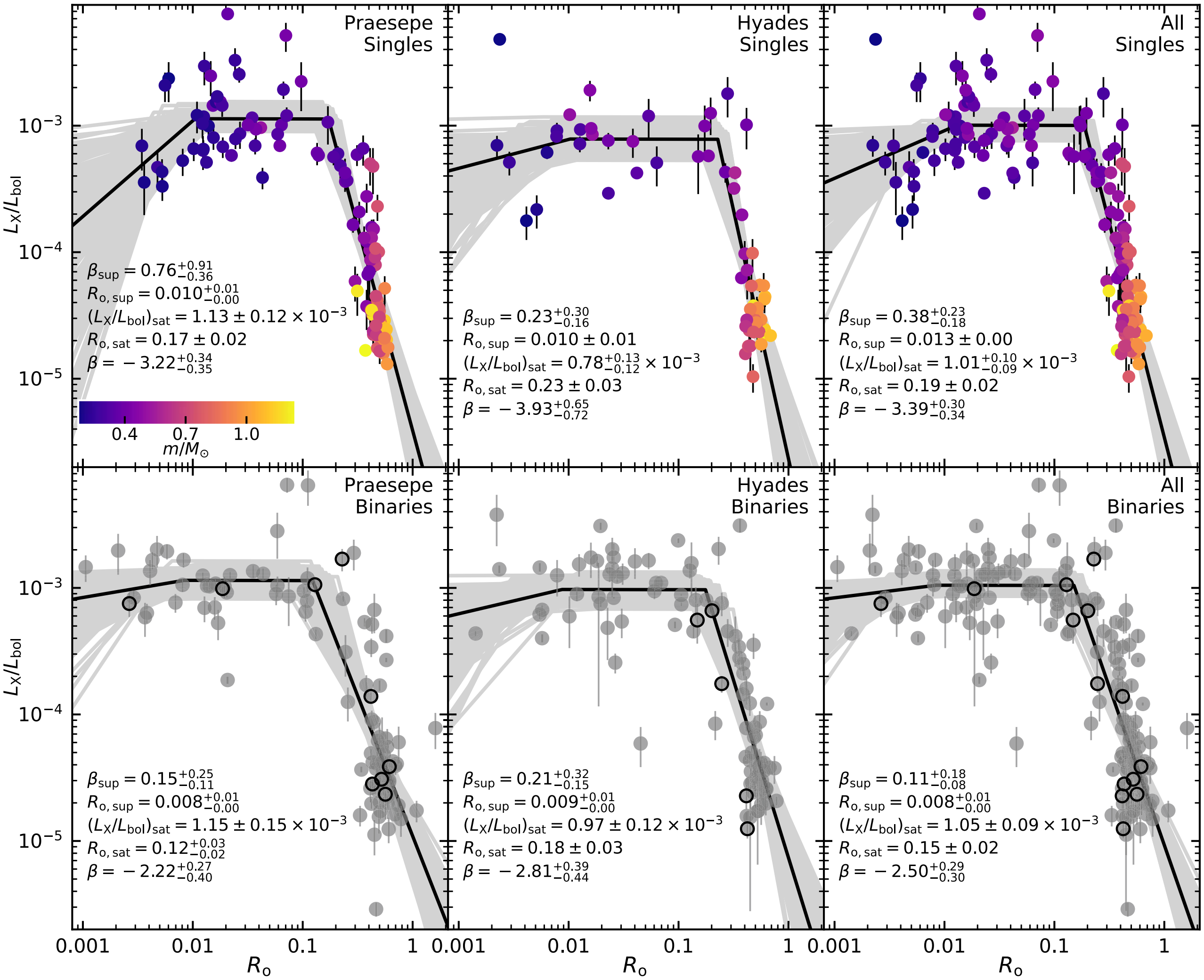

Figure 15. Same as Figure 12, but for a modified R_o–L_X/L_{bol} model that includes a secondary power law with index β_{sup} for $R_o < R_{o,sup}$, where $R_{o,sup}$ is the threshold R_o value between supersaturation and saturation. We find only tentative evidence for supersaturation in single stars with $R_o \lesssim 0.01$, for which the power-law index β_{sup} is distinct enough from zero.

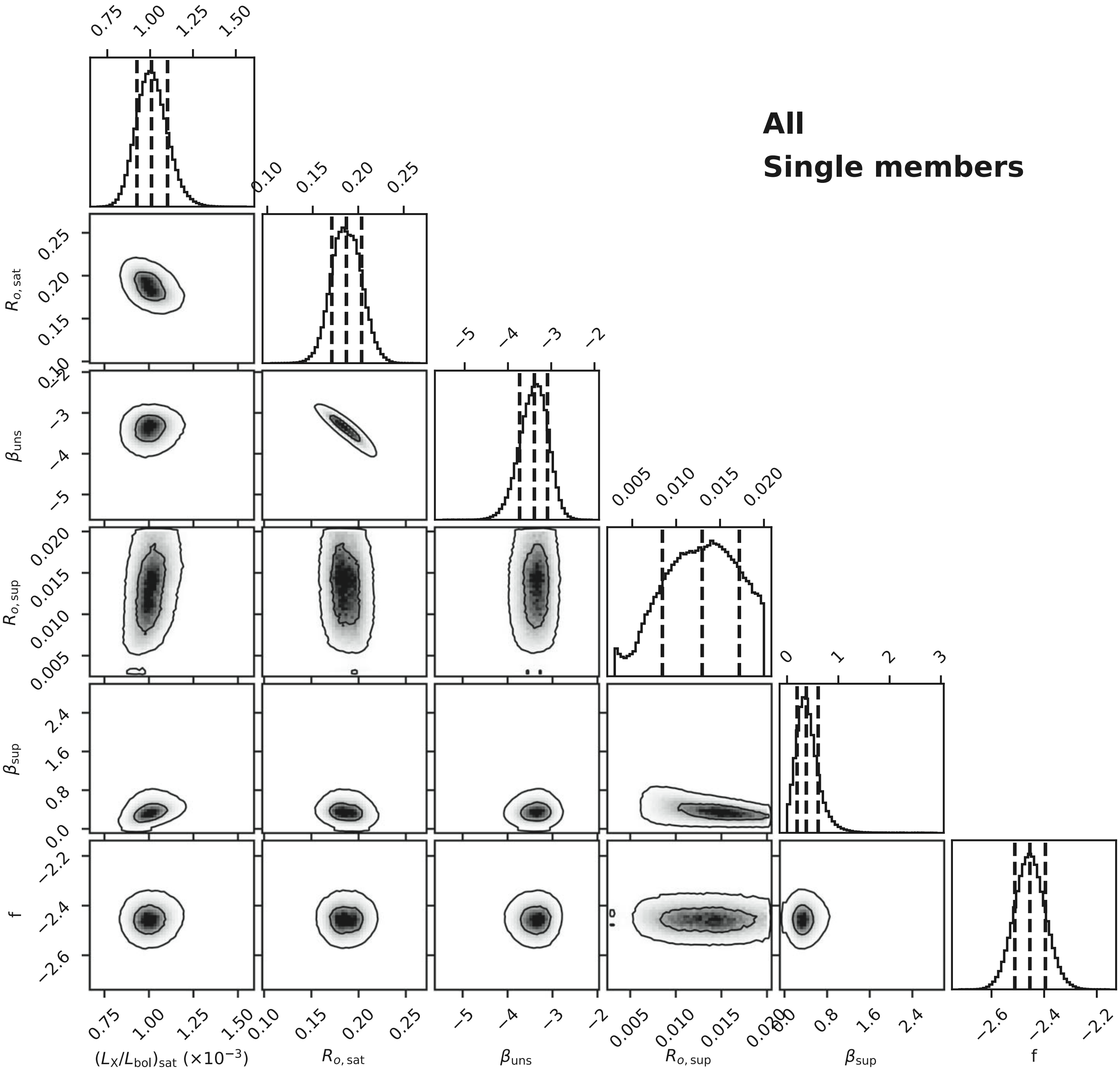

Figure 16. Same as Figure 14, but from the MCMC analysis of our modified R_o–L_X/L_{bol} model with supersaturation (see Section 5.3.2). The complete figure set, which includes an image for each of the six subsamples in Table 8, is available in the online journal.

(The complete figure set (6 images) is available.)

ORCID iDs

Alejandro Núñez https://orcid.org/0000-0002-8047-1982
Marcel A. Agüeros https://orcid.org/0000-0001-7077-3664
Kevin R. Covey https://orcid.org/0000-0001-6914-7797
Stephanie T. Douglas https://orcid.org/0000-0001-7371-2832
Jeremy J. Drake https://orcid.org/0000-0002-0210-2276
Rayna Rampalli https://orcid.org/0000-0001-7337-5936
Phillip A. Cargile https://orcid.org/0000-0002-1617-8917
Adam L. Kraus https://orcid.org/0000-0001-9811-568X
Nicholas M. Law https://orcid.org/0000-0001-9380-6457

References

Agüeros, M. A., Covey, K. R., Lemonias, J. J., et al. 2011, ApJ, 740, 110
Alexander, F., & Preibisch, T. 2012, A&A, 539, A64
Argiroffi, C., Caramazza, M., Micela, G., et al. 2016, A&A, 589, A113
Bailer-Jones, C. A. L., Rybizki, J., Fouesneau, M., Demleitner, M., & Andrae, R. 2021, AJ, 161, 147
Barnes, S. A. 2003a, ApJ, 586, 464
Barnes, S. A. 2003b, ApJL, 586, L145
Becker, A. C., Bochanski, J. J., Hawley, S. L., et al. 2011, ApJ, 731, 17
Belokurov, V., Penoyre, Z., Oh, S., et al. 2020, MNRAS, 496, 1922
Blackman, E. G., & Thomas, J. H. 2015, MNRAS, 446, L51

Böhm-Vitense, E., & Dettmann, T. 1980, ApJ, 236, 560
Böhm-Vitense, E., Robinson, R., Carpenter, K., & Mena-Werth, J. 2002, ApJ, 569, 941
Boller, T., Freyberg, M. J., Trümper, J., et al. 2016, A&A, 588, A103
Boudreault, S., Bailer-Jones, C. A. L., Goldman, B., Henning, T., & Caballero, J. A. 2010, A&A, 510, A27
Brinkman, A. C., Behar, E., Güdel, M., et al. 2001, A&A, 365, L324
Burke, D., Laurino, O., Wmclaugh, et al. 2021, sherpa/sherpa: Sherpa, v4.13.0, Zenodo, doi:10.5281/zenodo.4428938
Cantat-Gaudin, T., Jordi, C., Vallenari, A., et al. 2018, A&A, 618, A93
Cardini, D., & Cassatella, A. 2007, ApJ, 666, 393
Chabrier, G., & Baraffe, I. 1997, A&A, 327, 1039
Charbonneau, P. 2014, ARA&A, 52, 251
Cook, B. A., Williams, P. K. G., & Berger, E. 2014, ApJ, 785, 10
Counselman, C. C. I. 1973, ApJ, 180, 307
Deacon, N. R., & Kraus, A. L. 2020, MNRAS, 496, 5176
Dittmann, J. A., Irwin, J. M., Charbonneau, D., & Berta-Thompson, Z. K. 2014, ApJ, 784, 156
Douglas, S. T., Agüeros, M. A., Covey, K. R., et al. 2014, ApJ, 795, 161
Douglas, S. T., Agüeros, M. A., Covey, K. R., et al. 2016, ApJ, 822, 47
Douglas, S. T., Agüeros, M. A., Covey, K. R., & Kraus, A. 2017, ApJ, 842, 83
Douglas, S. T., Curtis, J. L., Agüeros, M. A., et al. 2019, ApJ, 879, 100
Drake, J. J., & Kashyap, V. 2001, ApJ, 547, 428
Drake, J. J., Laming, J. M., & Widing, K. G. 1997, ApJ, 478, 403
Drake, J. J., Marshall, H. L., Dreizler, S., et al. 2002, ApJ, 572, 996
Drake, J. J., Stern, R. A., Stringfellow, G., et al. 1996, ApJ, 469, 828
Evans, I. N., Primini, F. A., Miller, J. B., et al. 2020a, AAS Meeting Abstracts, 235, 154.05
Evans, P. A., Page, K. L., Osborne, J. P., et al. 2020b, ApJS, 247, 54
Fleming, D. P., Barnes, R., Davenport, J. R. A., & Luger, R. 2019, ApJ, 881, 88
Foreman-Mackey, D., Hogg, D. W., Lang, D., & Goodman, J. 2013, PASP, 125, 306
Freeman, P., Doe, S., & Siemiginowska, A. 2001, Proc. SPIE, 4477, 76
Freund, S., Robrade, J., Schneider, P. C., & Schmitt, J. H. M. M. 2020, A&A, 640, A66
Fruscione, A., McDowell, J. C., Allen, G. E., et al. 2006, Proc. SPIE, 6270, 1
Gaia Collaboration, Brown, A. G. A., Vallenari, A., et al. 2018a, A&A, 616, A1
Gaia Collaboration, Babusiaux, C., van Leeuwen, F., et al. 2018b, A&A, 616, A10
Gaia Collaboration, Brown, A. G. A., Vallenari, A., et al. 2021, A&A, 649, A1
Gabriel, C., Denby, M., Fyfe, D. J., et al. 2004, in ASP Conference Series, Vol. 314, Astronomical Data Analysis Software and Systems (ADASS) XIII, ed. F. Ochsenbein, M. G. Allen, & D. Egret (San Francisco, CA: ASP), 759
García-Alvarez, D., Drake, J. J., & Testa, P. 2009, in AIP Conf. Ser. 1094, 15th Cambridge Workshop on Cool Stars, Stellar Systems, and the Sun, ed. E. Stempels (Melville, NY: AIP), 796
Garmire, G. P., Bautz, M. W., Ford, P. G., Nousek, J. A., & Ricker, G. R. Jr. 2003, Proc. SPIE, 4851, 28
Gilman, P. A. 1983, ApJS, 53, 243
Goldman, B., Röser, S., Schilbach, E., et al. 2013, A&A, 559, A43
Güdel, M. 2007, LRSP, 4, 3
Howell, S. B., Sobeck, C., Haas, M., et al. 2014, PASP, 126, 398
Jackson, R. J., & Jeffries, R. D. 2010, MNRAS, 407, 465
James, D. J., Jardine, M. M., Jeffries, R. D., et al. 2000, MNRAS, 318, 1217
Jardine, M. 2004, A&A, 414, L5
Jardine, M., & Unruh, Y. C. 1999, A&A, 346, 883
Jeffries, R. D., Jackson, R. J., Briggs, K. R., Evans, P. A., & Pye, J. P. 2011, MNRAS, 411, 2099
Jones, B. F., & Cudworth, K. 1983, AJ, 88, 215
Jones, B. F., & Stauffer, J. R. 1991, AJ, 102, 1080
Jorissen, A. 2019, Mem. Soc. Astron. Italiana, 90, 395
Kains, N., Wyatt, M. C., & Greaves, J. S. 2011, MNRAS, 414, 2486
Kervella, P., Arenou, F., & Thévenin, F. 2022, A&A, 657, A7
Klein Wassink, W. J. 1927, PGro, 41, 1
Kochukhov, O. 2003, A&A, 404, 669
Kowalski, A. F., Hawley, S. L., Hilton, E. J., et al. 2009, AJ, 138, 633
Kraus, A. L., Douglas, S. T., Mann, A. W., et al. 2017, ApJ, 845, 72
Kraus, A. L., & Hillenbrand, L. A. 2007, AJ, 134, 2340
Kraus, A. L., Ireland, M. J., Huber, D., Mann, A. W., & Dupuy, T. J. 2016, AJ, 152, 8
Laming, J. M. 2015, LRSP, 12, 2
Lang, P., Jardine, M., Donati, J.-F., Morin, J., & Vidotto, A. 2012, MNRAS, 424, 1077
Law, N. M., Kulkarni, S. R., Dekany, R. G., et al. 2009, PASP, 121, 1395
Lawrence, A., Warren, S. J., Almaini, O., et al. 2007, MNRAS, 379, 1599
Lodieu, N., Boudreault, S., & Béjar, V. J. S. 2014, MNRAS, 445, 3908
Lodieu, N., Pérez-Garrido, A., Smart, R. L., & Silvotti, R. 2019a, A&A, 628, A66
Lodieu, N., Smart, R. L., Pérez-Garrido, A., & Silvotti, R. 2019b, A&A, 623, A35
Magaudda, E., Stelzer, B., Covey, K. R., et al. 2020, A&A, 638, A20
Mamajek, E. E., & Hillenbrand, L. A. 2008, ApJ, 687, 1264
Manjavacas, E., Lodieu, N., Béjar, V. J. S., et al. 2020, MNRAS, 491, 5925
Marsden, S. C., Carter, B. D., & Donati, J.-F. 2009, MNRAS, 399, 888
Meibom, S., & Mathieu, R. D. 2005, ApJ, 620, 970
Meibom, S., Mathieu, R. D., & Stassun, K. G. 2007, ApJL, 665, L155
Meingast, S., & Alves, J. 2019, A&A, 621, L3
Messina, S., Lanzafame, A. C., Malo, L., et al. 2017, A&A, 607, A3
Noyes, R. W., Weiss, N. O., & Vaughan, A. H. 1984, ApJ, 287, 769
Núñez, A., Agüeros, M. A., Covey, K. R., et al. 2015, ApJ, 809, 161
Núñez, A., Agüeros, M. A., Covey, K. R., & López-Morales, M. 2017, ApJ, 834, 176
Ochsenbein, F., Bauer, P., & Marcout, J. 2000, A&AS, 143, 23
Osten, R. A., Godet, O., Drake, S., et al. 2010, ApJ, 721, 785
Pallavicini, R., Golub, L., Rosner, R., et al. 1981, ApJ, 248, 279
Parker, E. N. 1993, ApJ, 408, 707
Pearce, L. A., Kraus, A. L., Dupuy, T. J., et al. 2020, ApJ, 894, 115
Pecaut, M. J., & Mamajek, E. E. 2013, ApJS, 208, 9
Penoyre, Z., Belokurov, V., Wyn Evans, N., Everall, A., & Koposov, S. E. 2020, MNRAS, 495, 321
Pérez-Garrido, A., Lodieu, N., Rebolo, R., & Chinchilla, P. 2018, A&A, 620, A130
Perryman, M. A. C., Lindegren, L., Kovalevsky, J., et al. 1997, A&A, 323, L49
Pizzolato, N., Maggio, A., Micela, G., Sciortino, S., & Ventura, P. 2003, A&A, 397, 147
Predehl, P., & Schmitt, J. H. M. M. 1995, A&A, 293, 889
Pye, J. P., Hodgkin, S. T., Stern, R. A., & Stauffer, J. R. 1994, MNRAS, 266, 798
Rampalli, R., Agüeros, M. A., Curtis, J. L., et al. 2021, ApJ, 921, 167
Randich, S. 2000, in ASP Conf. Ser. 198, Stellar Clusters and Associations: Convection, Rotation, and Dynamos, ed. R. Pallavicini, G. Micela, & S. Sciortino (San Francisco, CA: ASP), 401
Randich, S., Pasquini, L., & Pallavicini, R. 2000, A&A, 356, L25
Randich, S., & Schmitt, J. H. M. M. 1995, A&A, 298, 115
Randich, S., Schmitt, J. H. M. M., Prosser, C. F., & Stauffer, J. R. 1996, A&A, 305, 785
Rau, A., Kulkarni, S. R., Law, N. M., et al. 2009, PASP, 121, 1334
Rebull, L. M., Stauffer, J. R., Megeath, S. T., Hora, J. L., & Hartmann, L. 2006, ApJ, 646, 297
Reid, I. N., Hawley, S. L., & Gizis, J. E. 1995, AJ, 110, 1838
Riello, M., De Angeli, F., Evans, D. W., et al. 2021, A&A, 649, A3
Robert, J., Gagné, J., Artigau, É., et al. 2016, ApJ, 830, 144
ROSAT Consortium 2000, VizieR On-line Data Catalog: IX/30
ROSAT Scientific Team 2000, VizieR On-line Data Catalog: IX/28A
Röser, S., & Schilbach, E. 2019, A&A, 627, A4
Röser, S., Schilbach, E., & Goldman, B. 2019, A&A, 621, L2
Röser, S., Schilbach, E., Piskunov, A. E., Kharchenko, N. V., & Scholz, R.-D. 2011, A&A, 531, A92
Sanz-Forcada, J., Ribas, I., Micela, G., et al. 2010, A&A, 511, L8
Schlafly, E. F., & Finkbeiner, D. P. 2011, ApJ, 737, 103
Schneider, A. C., Windsor, J., Cushing, M. C., Kirkpatrick, J. D., & Shkolnik, E. L. 2017, AJ, 153, 196
Singh, K. P., Drake, S. A., Gotthelf, E. V., & White, N. E. 1999, ApJ, 512, 874
Skrutskie, M. F., Cutri, R. M., Stiening, R., et al. 2006, AJ, 131, 1163
Smith, R. K., Brickhouse, N. S., Liedahl, D. A., & Raymond, J. C. 2001, ApJ, 556, L91
Stauffer, J. R., Caillault, J.-P., Gagne, M., Prosser, C. F., & Hartmann, L. W. 1994, ApJS, 91, 625
Stauffer, J. R., Hartmann, L. W., Prosser, C. F., et al. 1997, ApJ, 479, 776
Stępień, K., Schmitt, J. H. M. M., & Voges, W. 2001, A&A, 370, 157
Stelzer, B., & Neuhäuser, R. 2001, A&A, 377, 538
Stelzer, B., Neuhäuser, R., & Hambaryan, V. 2000, A&A, 356, 949
Stern, R. A., Schmitt, J. H. M. M., & Kahabka, P. T. 1995, ApJ, 448, 683
Taylor, B. J. 2006, AJ, 132, 2453
Telleschi, A., Güdel, M., Briggs, K., et al. 2005, ApJ, 622, 653
Testa, P. 2010, SSRv, 157, 37
Testa, P., Drake, J. J., & Peres, G. 2004, ApJ, 617, 508
Testa, P., Saar, S. H., & Drake, J. J. 2015, RSPTA, 373, 20140259
Thiemann, H. B., Norton, A. J., & Kolb, U. C. 2020, PASA, 37, e042

van Leeuwen, J., Ferdman, R. D., Meyer, S., & Stairs, I. 2007, MNRAS, 374, 1437
Vikhlinin, A. 2001, Reducing ACIS Quiescent Background Using Very Faint Mode, 2010.11.15, https://cxc.harvard.edu/cal/Acis/Cal_prods/vfbkgrnd/
Vilhu, O. 1984, A&A, 133, 117
Voges, W., Aschenbach, B., Boller, T., et al. 1999, A&A, 349, 389
Walter, F. M., & Linsky, J. L. 1986, in ESA Special Publication, New Insights in Astrophysics. Eight Years of UV Astronomy with IUE, ed. E. J. Rolfe & R. Wilson, Vol. 263 (Paris: ESA), 103
Wang, S., & Chen, X. 2019, ApJ, 877, 116
Webb, N. A., Coriat, M., Traulsen, I., et al. 2020, A&A, 641, A136
Wolff, S. C., & Heasley, J. N. 1987, PASP, 99, 957
Wood, B. E., & Laming, J. M. 2013, ApJ, 768, 122
Wood, B. E., Laming, J. M., & Karovska, M. 2012, ApJ, 753, 76
Wood, B. E., & Linsky, J. L. 2010, ApJ, 717, 1279
Wright, N. J., & Drake, J. J. 2016, Natur, 535, 526
Wright, N. J., Drake, J. J., Mamajek, E. E., & Henry, G. W. 2011, ApJ, 743, 48
Wright, N. J., Newton, E. R., Williams, P. K. G., Drake, J. J., & Yadav, R. K. 2018, MNRAS, 479, 2351
Zahn, J.-P. 2008, in EAS Publications Series, ed. M.-J. Goupil & J.-P. Zahn, Vol. 29 (Geneva: European Astronomical Society), 67
Zhang, Z. H., Pinfield, D. J., Day-Jones, A. C., et al. 2010, MNRAS, 404, 1817
Ziegler, C., Law, N. M., Baranec, C., et al. 2018, AJ, 156, 259
Ziegler, C., Tokovinin, A., Briceño, C., et al. 2020, AJ, 159, 19